EXPERIMENTAL INVESTIGATION OF POINTING ERRORS ON DRONE-BASED FSO SYSTEMS

A Thesis

by

Anılcan Tosun

Submitted to the
Graduate School of Sciences and Engineering
In Partial Fulfillment of the Requirements for
the Degree of

Master of Science

in the
Department of Electrical and Electronics Engineering

Özyeğin University
December 2021

EXPERIMENTAL INVESTIGATION OF POINTING ERRORS ON DRONE-BASED FSO SYSTEMS

Approved by:

Professor Murat Uysal, Advisor
Department of Electrical and Electronics Engineering
Özyeğin University

Assistant Professor Kadir Durak
Department of Electrical and Electronics Engineering
Özyeğin University

Assistant Professor Vecdi Emre Levent
Department of Computer Engineering
Fenerbahçe University

Date Approved: 28 December 2021

to my mother and father

ABSTRACT

Airborne free-space optical (FSO) communication links can be efficiently used for backhaul/fronthaul needs of future cellular networks. Unlike terrestrial FSO links where a fixed connection between two buildings is considered, airborne FSO links bring unique challenges due to the mobility of the drone. In this thesis, an experimental study is carried out to demonstrate the effect of pointing errors in drone-based FSO systems. A supervised learning method is employed for tracking purpose of the FSO signal. Further, power measurements are taken, and the probability distribution of the received signal power is characterized. We further present comparisons between tracking and non-tracking cases and demonstrate the benefits of the tracking system. Motivated by these results, we then purse the second experimental campaign using a MEMS scanner. Furthermore, we investigate whether the studies in the literature match real-life situations. For this, quadcopter data taken from computer simulations are used, and after power measurements are taken by driving the MEMS scanner.

ÖZETÇE

Havadan serbest uzay optik haberleşme (FSO) bağlantıları, gelecekteki hücresel ağların arabağlanım ihtiyaçları için verimli bir şekilde kullanılabilir. İki bina arasında sabit bir bağlantı olarak düşünüldüğünde karasal FSO bağlantılarının aksine, havadan FSO bağlantıları dronun hareketliliği nedeniyle kendine özgü zorluklar getirir. Bu tezde, dron tabanlı FSO sistemlerinde hizalama hatalarının etkisini göstermek için deneysel bir çalışma gerçekleştiriyoruz. FSO sinyalinin izlenmesi amacıyla gözetimli bir öğrenme yöntemi kullanıyoruz. Güç ölçümleri alıyoruz ve alınan sinyal gücünün olasılık dağılımını karakterize ediyoruz. Ayrıca takipli ve takipsiz durumlar arasında karşılaştırmalar sunup takip sisteminin faydalarını gösteriyoruz. Bu sonuçlarla motive olarak, bir MEMS tarayıcı kullanarak ikinci deneysel süreci takip ediyoruz. Buna ek olarak, literatürdeki çalışmaların gerçek hayatta olan durumlarıyla uyuşup uyuşmadığını araştırıyoruz. Bunun için bilgisayar simülasyonlarından alınan dron verilerini kullanılıyor ve sonrasında MEMS tarayıcıyı sürerek güç ölçümleri yapıyoruz.

ACKNOWLEDGEMENTS

I want to express my appreciation to my advisor, Prof. Murat Uysal, for his support, guidance, suggestions, and generosity during this experience as an MSc student. The work on this thesis would not have been possible without the opportunity and support he provided.

I am totally grateful for the technical and non-technical discussions with my colleagues in the Center of Excellence for Optical Wireless Communications Technologies (OKATEM). I have as well enjoyed the collaboration and fruitful conversations with the CT&T research group. I would also like to thank the one and only Mohammed Elamassie, who did not hesitate to spend his time answering all my questions, whether they were simple or not.

To my fellas at Hyperion Technologies, thank you all for the stimulating discussions, sleepless nights, endeavoring without ceasing before deadlines, and for all the fun we had together. I have sincere gratitude to my friend and colleague Burak Kebapci for his endless support and great friendship.

I would like to thank my uncle, Kurt Ebik. There is no way to express how much it means to me to have such an amazing figure in my life. He has always been ready to lend a helping hand my entire life. I am incredibly proud to have followed in his footsteps, and as a role model, he has always demonstrated how to overcome difficulties and achieve success.

My warmest gratitude goes to my beloved parents, Erdal and Serife, who have always supported me unconditionally throughout my life. I will forever be indebted to them for their sacrifices and endless patience. It was their love that kept me motivated whenever I got weary. I would like to especially thank my sister, Beste, for being the best sibling anyone could ever have.

ACRONYMS

2D	Two-dimensional
3D	Three-dimensional
5G	The Fifth Generation of Cellular Networks
6G	The Sixth Generation of Cellular Networks
AI	Artificial Intelligence
AlN	Aluminum Nitride
CCW	Counterclockwise
CW	Clockwise
EMA	Electromagnetic
ESA	Electrostatic
FPS	Frames Per Second
FSO	Free-Space Optical
Gbps	Gigabits Per Second
GPS	Global Positioning System
HSV	Hue, Saturation, and Value
IMU	Inertial Measurement Unit
IoT	Internet of Things
IR	Infrared
LED	Light Emitting Diode
LOS	Line of Sight
M2M	Machine-to-machine
MEMS	Microelectromechanical Systems
OOP	Object-oriented Programming
OWC	Optical Wireless Communication
PAT	Pointing, Acquisition, and Tracking

PC	Personal Computer
PDF	Probability Density Function
PEA	Piezoelectric
PID	Proportional, Integral and Derivative
PYPL	Popularity of Programming Language
PZT	Lead Zirconate Titanate
QoS	Quality of Service
RF	Radio Frequency
RGB	Red, Green, and Blue
ROS	Robot Operating System
SDF	Simulation Description Format
SDK	Software Development Kit
UAV	Unmanned Aerial Vehicle
UDP	User Datagram Protocol
URDF	Unified Robotic Description Format
UV	Ultraviolet
V2V	Vehicle-to-vehicle
VLC	Visible Light Communication
WLAN	Wireless Local Area Network
XML	Extensible Markup Language
ZnO	Zinc Oxide

TABLE OF CONTENTS

LIST OF TABLES

LIST OF FIGURES

CHAPTER I

INTRODUCTION

1.1 Background and Motivation

The new digital age takes our lives to another level than ever before. Various transformations and accelerated digitalization are witnessed in every sector and every field. Wireless connectivity is one of the pivots of this transition. According to Cisco's Annual Internet Report (2018-2023), "nearly two-thirds of the global population will have Internet access by 2023," and "Machine-to-machine (M2M) connections will be half of the global connected devices and connections by 2023" [1]. The increasing demand for better performance, reliability, and usability naturally makes the developments in this field the focus. As a result of the substantial progress on Artificial Intelligence (AI), Internet of Things (IoT) devices, and M2M communication over the past few years, The Fifth Generation of Cellular Networks (5G) is designed to meet the requirements for reliable communication with these promising topics. As of November 2021, more than 180 service providers have launched commercial 5G services, which reach around 570 million subscribers and estimations are more than 660 million by the end of 2021 globally (see Table 1) [2].

	Forecasted for 2016 (Predictions made in November 2011)	**Actual 2016**	**Forecasted for 2021 (Predictions made in November 2015)**	**Estimates for 2021 (End of year figures)**
Mobile subscriptions	8.4 bn	7.4 bn	9.1 bn	8.1 bn
Mobile PC/tablet subscriptions	550 m	180 m	350 m	300 m
Smartphone subscriptions	2.6 bn	3.7 bn	6.4 bn	6.3 bn
4G subscriptions	510 m	2.0 bn	4.1 bn	4.7 bn
5G subscriptions	-	-	150 m	660 m
Average Traffic per Smartphone	800 MB/m	1.9 GB/m	8.5 GB/m	114.4 GB/m
Total Mobile Traffic	4.6 EB/m	6.7 EB/m	51 EB/m	65 EB/m

Table 1: Comparison of forecasts vs. up-to-date data

It is another reality that the developments in wireless connectivity will not be limited to 5G. New technologies are applied much faster than in the past, and early research has begun on The Sixth Generation of Cellular Networks (6G), the likely successor of 5G. While trying to fulfill ubiquitous wireless connectivity, maintaining Quality of Service (QoS) with existing infrastructure is challenging. For example, backhaul networks for the next generation of wireless require higher spectral efficiency and a vast number of devices to be integrated into the core network. Therefore, the small cell backhaul/fronthaul deployments are crucial in the next generation of wireless networks to overcome the challenges. Even though small cells bring additional complexity to the design of the network, they promise a considerably cost-effective solution in comparison to macro cell base stations. Small cells are low-power wireless network base stations which densely utilized and operable up to a few kilometers. They can be deployed in streets, university campuses, urban and rural areas, and places where temporary communication solutions are needed, such as sports events, disaster areas. Although wired backhaul/fronthaul solutions are considered state-of-the-art, the cost of infrastructure makes wireless solutions stand out [3–6].

One of the most prominent solutions with promising features is Free-Space Optical (FSO) wireless communication when considering small cell backhaul solutions. Many companies both develop and sell point-to-point FSO products on the market. However, the integration of FSO systems as a small cell backhaul is a relatively new concept, and very few companies offer products to the market. It is projected that by 2030 the deployed FSO systems will increase extensively. Alternative to point-to-point FSO systems, another potential application can be the integration of FSO systems on Unmanned Aerial Vehicles (UAVs), commonly known as drones. With the advent of low-cost, easy to access, and significantly enhanced drones, they became a subject undergoing intense study by researchers [7–10].

In this thesis, in order to contribute to the studies in this field, the pointing error, which is considered one of the biggest challenges of the possible implementation of drone-enabled FSO systems as a fronthaul/backhaul solution or a mobile communication terminal, is experimentally investigated.

1.2 Overview of Free-space Optical Wireless Communication

Wireless communication technology has spread considerably faster than anybody could have predicted thirty years ago and has become the key factor of modern civilization. It is an undeniable fact that wireless Radio Frequency (RF) devices and systems are essential in daily life. Therefore, when the term wireless is mentioned, RF comes to one's mind right off as if it is synonymous with RF technologies. Although it seems like RF technologies have already reached the level of maturity, developments in this field still continue to grow and develop. However, due to the demand that started to exceed the limits of the RF band in the electromagnetic spectrum, the need to go beyond the RF spectrum in wireless communication emerged [11]. Optical Wireless Communication (OWC) is a wireless communication technology using electromagnetic waves within the optical range of the spectrum which can be divided into three distinct categories: Visible Light Communication (VLC), Infrared (IR), and Ultraviolet (UV), see Figure 1 [12].

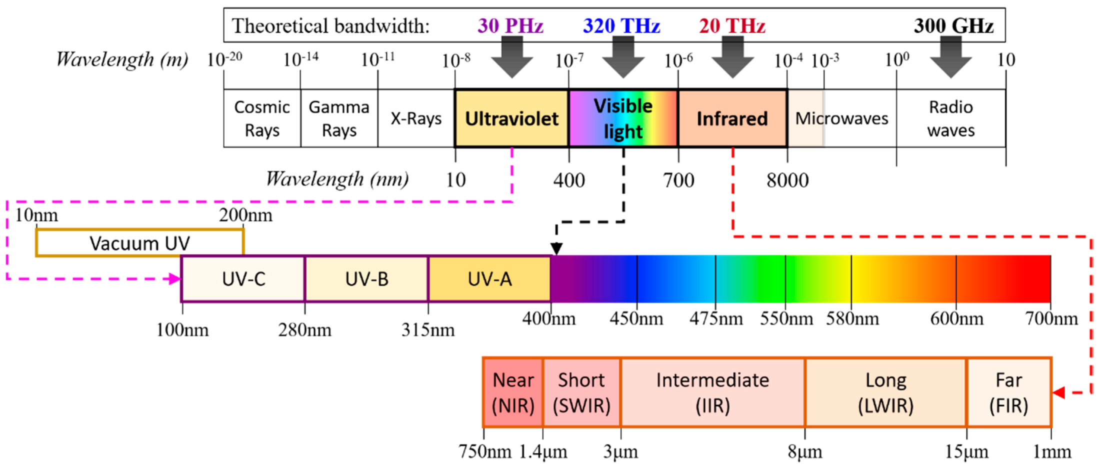

Figure 1: The Electromagnetic Spectrum

Historically, ancient peoples benefited from fire, smoke, and sunlight as an ingenious way of communication, and this can be considered as a primitive form of OWC. Despite some debates about other kinds of ancient optical signaling that existed before, Carl Friedrich Gauss' heliograph, which has been accepted in the literature as the first heliographic device, was used as a part of geodetic work in 1810. Afterward, in 1880, Alexander Graham Bell invented the wireless communication system, the photophone, which he called his greatest invention. This photophone was able to transmit voice signals across a distance of 200 meters using a simple optical setup which allows sending the vibrations reflected by sunlight. In the past, as in the present, military needs have always been a major impact on the development of technology and science. Until the 1950s, American and German military laboratories pursued developing electric arc lights for optical communication. The first contemporary OWC works are begun to appear right after the invention of the laser in 1960 by Theodore Maiman of Hughes Research Laboratories based on the theoretical work of Charles Hard Townes and Arthur Leonard Schawlow. In other words, the invention of the laser was a giant leap for OWC as it is in today's technological developments [13–15].

RF technologies are prevalent because, considering the variety of usage areas and applicability, technological developments in the past have fed that subject more than OWC, but by looking at today, this phenomenon has started to change. The increase in quality in the manufacturing of more sensitive and feasible optical elements, the widespread use of fiber optics, and the anticipation that Light Emitting Diodes (LEDs) are the ultimate light source in the future have made OWC a strong candidate. Rather than indoor illumination, LEDs are also extensively used in street lighting, traffic signs, and car headlights. Therefore, using LEDs as a short- and medium-range VLC solution makes sense. It can be effectively applied in areas such as Wireless Local Area Network (WLAN), Vehicle-to-vehicle (V2V), M2M, aerial and underwater communication. OWC can be examined in five different categories according to usage areas, and transmission range in Table 2 on the following page [11].

Unlike LEDs, which can be used more efficiently at short and medium-range, lasers

Category	Range	Application
Ultra Short Range OWC	mm	Chip-to-chip Communication
Short Range OWC	cm	WAN Applications
Medium Range OWC	m	Indoor VLC, V2V, M2M
Long Range OWC	km	Inter-building Communication
Ultra Long Range OWC	>10.000 km	Inter-satellite Communication

Table 2: OWC categories

can be used in all categories stated in Table 2. In the literature, OWC links are widely referred as FSO communication which is an optical communication technology that uses lasers for transmitting data through the atmosphere. FSO systems have been at the center of attraction for wireless communication in recent years with their wide-range applications and advantages. Achieving high data rates up to 10 Gigabits Per Second (Gbps) through immensely secure communication is one of the advantages of this technology. As previously stated, the insufficient bandwidth problem in wireless RF communication technologies highlights the significance of FSO, which has 2600 times larger spectrum when infrared and visible light are combined. This spectrum is license-free so that the system can be operated worldwide without the authorization of any institution. Moreover, FSO systems are more robust to electromagnetic interference since very narrow laser beams are used. Besides fiber-optic communication, FSO systems are easy to deploy, and the infrastructure costs of the systems are substantially less. The fundamental differences between FSO and RF systems are summarized in Table 3 on the following page.

FSO communication systems can be used in various application areas, including enterprise/campus connectivity, cellular networks backhauling/fronthauling, and airborne communications. Nowadays, homogeneous networks, comprised of devices connected with similar configurations and protocols, have been old-fashioned and left their place to heterogeneous networks. The upsurge in demands from the diverse network traffic in corporate, schools/universities, and public places overloads conventional connections. In this context, ultra-high-speed connections can be achieved by integrating FSO systems at different locations as part of the network. Such high-performance FSO systems

	FSO Systems	RF Systems
Bandwidth regulations	Unlicensed	Licensed
Security	High	Low
Electromagnetic interference	No	Yes
Wall penetration	No	Yes
Available bandwidth	Very high	Low
Noise sources	Sun and ambient light	Other systems and users
Eye safety	Required	N/A
Power loss	915 MHz 92dB/km 2.4 GHz 100dB/km 5.7 GHz 108dB/km	Clear 5-15 dB/km Rain 20-50 dB/km Snow 50-150 dB/km Fog 50-300 dB/km

Table 3: Comparison between FSO and RF systems

are also projected to be implemented in the backhaul of next-generation cellular networks enabling seamless connectivity. Terrestrial 5G network coverage may fall short of the requirements for the rural area, disaster investigation, airborne and maritime communications; hence, the proliferation of mobile FSO systems may be a solution for such challenging communications [16–19].

1.3 Airbone FSO Communication

As a definition, UAVs are a type of aircraft operated without a pilot, crew, or passengers on board. An operator on the ground can remotely control it, or pre-defined flight plans can independently control the flight. Over the last decades, UAVs have been primarily used for military purposes, and today, they are in the limelight for non-military applications as well. For example, UAVs have already become a common method of choice for law enforcement, wildfire management, hurricane monitoring, and data collection. A list showing the wide range of applications of UAVs is in Table 4 on the next page [20–22].

Civil Applications	• Agriculture • Archaeology • Cargo • Construction • Filmmaking • Healthcare • Hobby and recreational use • Law enforcement • Manufacturing • Scientific research • Search and rescue • Surveillance
Military Applications	• Bomb disposal • Radar jamming • Reconnaissance • RF Relay • Shadowing enemy fleets • Surveillance • Warfare

Table 4: Application of UAVs

Even though there is no universal standard for classifying UAVs, it is possible to see that they are classified according to their size, weight, range, and durability. As shown in Table 5, UAVs can be divided into four categories based on their size [23]. As the development of advanced chips, sensors, and control technology progressed, UAVs became smaller, affordable, and more capable. Starting from this part of the section, the terms "drone" and "quadcopter" will be used instead of UAVs, which resemble rather small and compact forms of UAVs, in accordance with the scope of this study.

Category	**Maximum Dimension**
Ultra-small (NAV)	<7.5 cm
Very Small (MAV)	7.5–15 cm
Small	15–200 cm
Medium	2–10 m
Large	>10 m

Table 5: UAV classification

The majority of the studies of FSO communications are mainly limited to terrestrial and space links [16, 17]. However, in alignment with the increasing deployment of drones, there has been growing attention on airborne FSO systems [24]. Drone-based FSO systems have also attracted the attention of big technology companies such as Facebook, Google, and Airbus. They have successfully demonstrated a massive-scale implementation of this emerging technology to provide Internet to rural and remote regions [25–27].

FSO communication systems are restricted to Line of Sight (LOS) for successful transmission, and environmental factors such as mountains, buildings, areas surrounded by water are not always feasible for terrestrial links. Second, it is known that FSO systems are highly affected by atmospheric turbulence. Specifically, this becomes more of a problem as the distance between source and destination increases [28]. As a solution to this problem, having a drone-mounted FSO relay can be efficiently integrated among other fixed relays for backhaul/fronthaul needs of cellular networks. The ability of variable link distance in drone-based FSO systems also brings advantages in terms of network performance. These systems might be especially useful in urban areas to provide backhaul for the small cell base stations, which will be commonly deployed in 5G cellular networks [29].

Not only an FSO transceiver sends the signal towards a base station, but also the idea of hovering drones equipped with an FSO transceiver may form an aerial backbone in the sky. These aerial backbone links are especially effective in rural regions having no optical fiber infrastructure [30]. In another potential application, a hybrid system such as mm-wave/FSO could be used together. Airborne hybrid FSO, with the complementary features of two or more communication systems and the advantages of drones' mobility, can be one of the most prominent technologies of the future [31–33].

Considering all the possible applications together, drone-based FSO systems can be categorized under three main categories, as shown in Figure 2 on the next page:

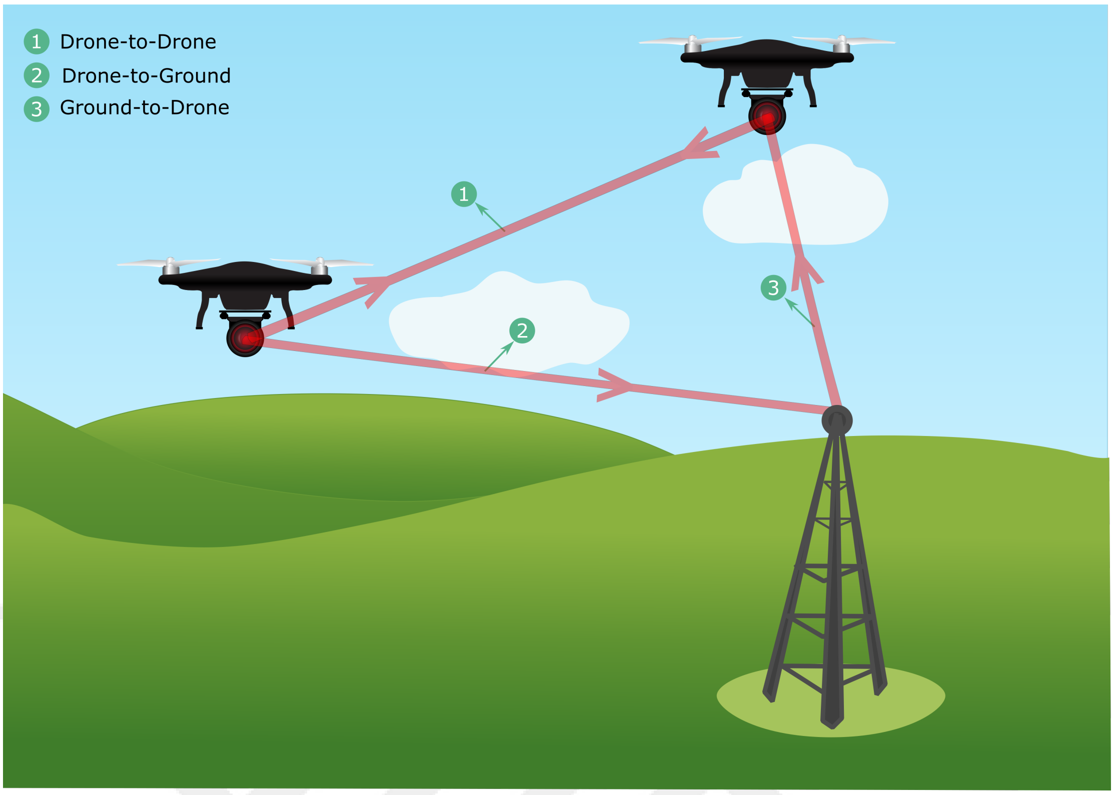

Figure 2: Drone-based FSO communication scenarios

1.4 Related Works

Unlike terrestrial FSO links where a fixed connection between two distinct locations (e.g., buildings, poles, etc.) is considered, airborne FSO links bring unique challenges due to the mobility of the drone. Drones are capable of freely moving in 3D (three-dimensional) space. The most critical challenge is the pointing error induced by the hovering drone. It is known that pointing errors take place also in terrestrial FSO links due to building sway [34, 35]. However, unlike building sway, where the buildings exhibit limited movement due to wind loads and thermal expansion, the airborne FSO link suffers significant variations in both the position and the orientation of the hovering drone. Random fluctuations of the transceiver positions lead to a spontaneous geometric loss effectively resulting in fading effect. There are some recent theoretical studies [36–38] to characterize the impact of pointing errors in drone-based FSO links; however, to the best of our knowledge, no experimental study is yet available in the literature to explore such effects.

1.5 Thesis Structure and Contributions

The remainder of the thesis is organized as follows: In Chapter 2, we employ a quadcopter equipped with a laser transmitter. Although the drone is equipped with a vision positioning system and multiple sensors, stabilization accuracy in the hovering state is not sufficiently high for FSO link alignments causing interruptions in link connectivity. In an effort to avoid link interruptions, we employ a simple machine-learning assisted tracking system. For this purpose, we use a computer as a ground station for controlling the drone. While the drone hovers, the video of the receive side is recorded and transferred to the ground station in real-time using the Wi-Fi connection. The recorded video is processed at the ground station based on Haar feature-based cascade classification [39] which is a supervised learning method used to detect the object for which it was trained. Control commands are then sent to the drone to adjust its position for maintaining the FSO link. We take power measurements and characterize the probability distribution of the received signal power. Our measurements demonstrate that the tracking system maximizes the received power, and the pointing error is significantly reduced, providing a more stable connection.

In Chapter 3, we employ a Microelectromechanical Systems (MEMS) scanner to reduce the impact of environmental conditions, e.g., reflective surfaces, indoor lighting, RF interference. Using a MEMS scanner in the experimental setup gives us a chance to examine further the misalignment caused by the hovering drone without an active tracking mechanism. In addition to the MEMS scanner, we take advantage of computer simulations in different scenarios. Through the Robot Operating System (ROS) and Gazebo, we have simulated drone models with realistic sensors and parameters that can deliver the closest results to the real world. We then emulate the movement data of the drone by controlling the MEMS scanner with MATLAB. In MATLAB, control commands are sent to the MEMS scanner via the serial port interface on the Personal Computer (PC) to adjust the position of the mirror. The laser beam is diverted to the power sensor by adjusting the position of the MEMS mirror. Under these conditions, power measurements are collected, and the probability distribution of the received signal power is characterized.

Finally, in Chapter 4, we present the conclusion of our works and provide an insight into future works.

CHAPTER II

QUADCOPTER EXPERIMENT

2.1 Drones

Drone technology has evolved rapidly as the versatility of electronic and mechanical components, and the intelligence of software systems become better in quality. Moreover, it is possible to have these fancy devices without spending sky-high money. Many hobbyists and students make their own drones by using Three-dimensional (3D) printed frames, open-source software, and hardware [40].

A controllable flying drone requires an embedded flight controller, a body frame, a motor, and a propeller attached to the motor at a minimum. Although reducing the number of propellers is directly proportional to the power consumption, at least four propellers are generally preferred for a more stable and capable drone. Propellers generate the lift force when the motors start rotating, and they also create the angular momentum which causes the rotation. A quadcopter has six degrees of freedom which they can move vertically, longitudinally, laterally, and exhibits roll, pitch, and yaw movements among each axis rotationally [41].

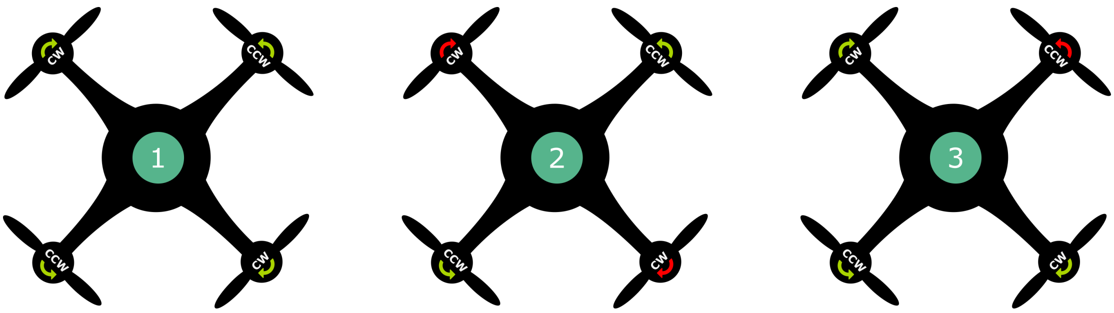

Figure 3: The movement and principal axis of a drone

As illustrated in Figure 3 on the preceding page:

1. By supplying equal thrust to all four rotors, a drone can hover or alter its altitude.

2. A drone's yaw is controlled by increasing the thrust applied to rotors moving in the same direction, i.e., red Clockwise (CW) arrows.

3. A drone's pitch or roll is controlled by increasing the trust applied to one rotor (e.g., green Counterclockwise (CCW) arrow) and giving the diagonally opposite rotor less thrust.

2.2 *DJI Tello*

In our experimental study, DJI Tello was chosen. One of the most important reasons here is that the DJI company presents Tello's own Software Development Kit (SDK). The SDK allows users to connect to the quadcopter via a 2.4 GHz Wi-Fi connection through a User Datagram Protocol (UDP) port, send control commands to the quadcopter, and receive status and sensor information from the quadcopter. It has a maximum flight duration of 13 minutes and a maximum flight distance of 100 m. The quadcopter is also equipped with a range finder, barometer, temperature, infrared vision sensors, and a video camera. A detailed diagram is given in Figure 4 [42].

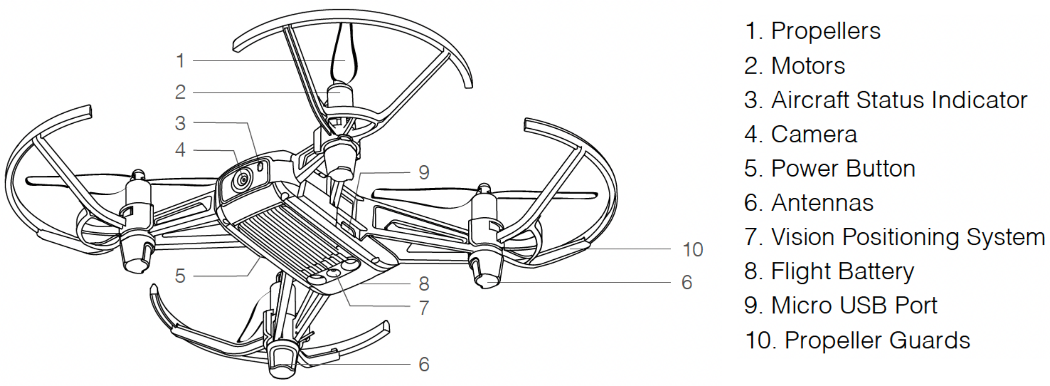

Figure 4: DJI Tello aircraft diagram

The advantage of having this SDK out-of-the-box, users can perform their own tasks on the drone without dealing with complex control algorithms. For example, sending the command ”up 20” over the UDP port connection allows the drone to move 20 cm upwards. Moreover, whether the drone executes the command or not can be checked with the response coming back from the UDP port [?].

Many mid-range drones commonly available on the market are integrated with Global Positioning System (GPS) systems. GPS signals are used to determine the speed and position of drones based on time more precisely, but they are not very efficient for indoor use. Tello does not have GPS; however, it is packed with a vision positioning system and advanced flight controller, making it more suitable for indoor use. The quadcopter’s current position is determined via the visual positioning system. The Tello can fly more accurately indoors or outdoors in windless circumstances with the help of the visual positioning system. A camera and a 3D infrared module are the major components of the vision positioning system. This positioning system ensures that the drone’s current position in the air is kept as stable as possible. The term hovering is used for aircraft which stay in the same position in the air. The performance of this system is directly related to the surface, which is being flown over. Flying over monochrome, reflective, and repetitive textured surfaces alongside a too dark or bright environment cause stability problems [42, 43].

An Inertial Measurement Unit (IMU) is an electronic component that uses accelerometers, gyroscopes, and magnetometers to determine the orientation and velocity of the drone. IMUs are essential components in unmanned aerial systems that directly impact the performance of the control, stabilization, and guidance. In addition to this, filters are also important for stabilization performance. IMU sensors are subjected to various noises so that the sensor signal is also affected. As a result, hardware and software-based filters are required to acquire high-accuracy sensor measurements. Although the ideal sensors are designed with the best filters, when aerodynamic effects and mechanical vibrations are added to the system, it is almost impossible for the drones to hover in the air without drifting. For example, in case of drift or sudden wind effect, the flight controller tries to keep the drone stable in its final position since IMUs accumulate errors [44]. In other words, this is a misalignment of FSO transceivers. This is why it seems unrealistic to apply FSO systems to drones without using any feedback mechanism. Therefore, a Pointing, Acquisition, and Tracking (PAT) system is necessary for drones to overcome this problem.

PAT mechanisms eliminate pointing errors in FSO communications systems by continuously assessing system-wide performance indicators such as received signal power and the pair device's position. These mechanisms are commonly used in fixed and mobile FSO and consist of elements such as gimbals, mirrors, or adaptive optics. These types of mechanisms are often bulky and large, thus introducing an additional constraint in drone-based FSO systems [45].

Implementation of PAT seems to be challenging, especially considering the size of small drones like the Tello and other mid-range drones. As a solution, the cameras seen in almost every drone today can be a key element for the development of an alternative system to PAT mechanisms. A tracking system can be developed using computer vision and image processing technology.

2.3 *Software*

2.3.1 OpenCV

Computer vision is a scientific field that studies how computers can perceive data taken from photos or videos by manipulating then retrieving information from them. In the age of artificial intelligence, there is hardly any field of AI where computer vision is not applicable. OpenCV is an open-source real-time computer vision programming framework under the permissive software license, which can be used commercially and academically. More than 2500 optimized algorithms are included in the OpenCV library, which contains modern computer vision and machine learning techniques. These algorithms can be used to detect pre-defined objects, extract the models of the objects and automatically contour the boundaries in the scene. The OpenCV library can be installed on any platform, such as desktop or server platforms running Windows, macOS, or Linux. Although OpenCV is written in C and C ++, it has Java, Python, and MATLAB interfaces. In this thesis, OpenCV was preferred since a real-time application was developed, and computational resources should be used very efficiently [46].

2.3.2 Haar-cascade Classification

Haar Cascade classification is a supervised learning method to detect and identify the object within a short amount of time while achieving pretty high accuracy. In this method, the cascade function is trained to distinguish weak classifiers using a multitude of positive and negative images. After the training, the cascade function is used to detect objects. The higher the number of images in training, the better the results, which causes higher consumption of computational resources and longer computation time. Positive images contain the object that must be detected, while negative images do not contain the desired object but help eliminate similar objects, environment, etc. [39].

In our experiment, 15 positive and 3000 negative images are prepared for training purposes, as shown in Figure 5. A mobile phone with a high-resolution camera was used to capture images of the object to be tracked from different perspectives. Negative images were selected from the ImageNet website [47], an extensive image database designed for use in object recognition.

(a) (b)

Figure 5: Sample of a) positive and b) negative image

Haar cascade features manipulate an area within the image rather than calculating the individual pixels directly. There are two-rectangle, three-rectangle, and four-rectangle features, as shown in Figure 6 on the next page. The areas have the same size rectangles but are divided equally into dark and light, horizontally or vertically adjacent

Rank	Change	Language	Share
1		Python	30.21%
2		Java	17.82%
3		JavaScript	9.16%
4		C#	7.53%
5		C/C	6.82%
6		PHP	5.84%
7		R	3.81%
8	↑	Swift	2.03%
9	↓	ObjectiveC	2.02%
10	↑	Matlab	1.73%

Table 6: Popularity of Programming Language by December 2021

regions. The weight of the rectangle area is computed by adding light regions and subtracting the dark regions. This is exactly the importance of using this method in terms of speed and resources because the additions and subtractions are significantly more efficient than multiplications and divisions [39, 48].

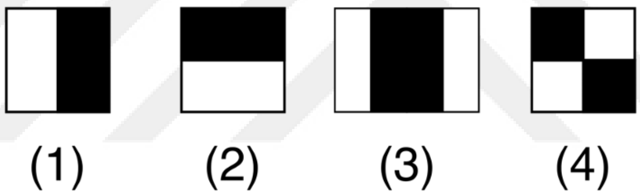

Figure 6: Haar cascade features

All of these calculations can be easily done by using the following OpenCV applications.

- opencv_createsamples
- opencv_traincascade

2.3.3 Python

According to the Popularity of Programming Language (PYPL) index, as of December 2021, Python is the most popular programming language and has grown the most in the last 5 years [49]. The top 10 programming languages in the list are in Table 6.

Python is an interpreted programming language that is not compiled before executing, and this gives the community a faster application development chance. Python supports the development very usefully from the start of the coding process until the test and debugging. For example, the debugger raises an exception instead of causing a segmentation fault when it catches a bug. Python has a wide range of good features supporting functional and structured methods such as Object-oriented Programming (OOP) [50].

Some Python features are:

- Easy-to-learn
- Easy-to-debug
- Easy-to-integrate
- Fast prototyping
- Vast open-source modules and packages
- Supports multiple hardware platforms

We require such a software program that perfectly matches the above features in order to achieve more productivity in this thesis. Therefore, choosing a compatible language such as Python programming language was inevitable.

2.3.4 Computer Vision Assisted Tracking System

As mentioned earlier, the tracking system is crucial in drone-based FSO communication systems due to the LOS connection requirement and the instability of drones. The tracking system represented in this thesis can be more advantageous than other PAT systems since it is software-oriented contrary to mechanical counterparts.

Before starting to develop the image processing algorithm, which objects to track are determined. The set of objects tracked with image processing contains a black background paper with a white circle in the center, Figure 7(a) on the next page, and the lens and power meter as a part of the receiver equipment, Figure 7(b) on the following page.

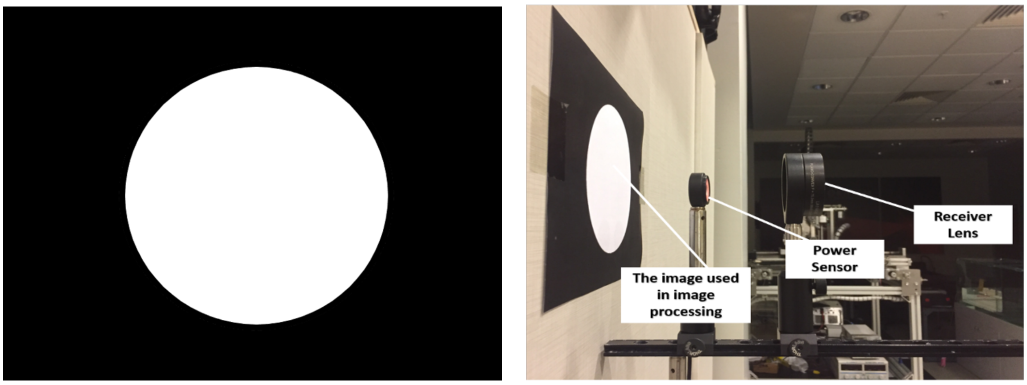

(a) (b)

Figure 7: The set of objects tracked with image processing

The development of the tracking software starts with defining the position of the drone on the x-axis, Figure 8 on the next page. For this, we captured the images from the front camera of the drone at 3 distances, where we will perform the experiment. The distance here refers to the distance between the laser on the drone and the receiving lens. Recording these images is to ensure that the drone remains stable at the desired distance for the experiment, according to the size of the objects monitored on the receiver side via the drone's camera. At this stage, we need to control the drone's back and forth movement in the x-axis. If the object is smaller than the frame determined by the distance from the pre-recorded images, the drone should move in the +x direction to hover at the required distance. On the contrary, the drone should move in the -x direction if the object is larger than the frame. These movements in the +x and -x directions prevent the drone from drifting as a result of the errors from the sensors.

For an FSO system to work at its best, LOS propagation must be provided so that the center of the beam emitted from the laser source and the detector must coincide. While developing the tracking software, one of the key performance indicators was to satisfy LOS condition for good measure. In order to compensate for the pointing error caused by the hovering drone in the experimental setup, it is necessary to control the movements in the y and z axes as well. Hence, the center of the frame that is drawn to determine the distance in the previous stage is marked with a red marker. This red marker is also the center of our receiver lens and detector. Given that the center of the laser beam merges with this red marker, it causes the system to function optimally, but any misalignment results in performance degradation. For this reason, the laser beam must be constantly tracked and returned to the red marker whenever the misalignment occurs.

Figure 8: DJI Tello axes

The first step is to get a single frame as an image from the video stream coming from the drone's camera. Images are described in the Red, Green, and Blue (RGB) color space in OpenCV, and the amount of red, green, and blue components constitute the RGB vector of the images. However, Hue, Saturation, and Value (HSV) color space gives more precise and accurate results than RGB for color thresholding. Because, unlike RGB, the colors can be distinguished more clearly by adjusting the hue value. The value ranges for hue, saturation, and value in OpenCV are [0-179], [0-255], and [0-255], respectively. The definitions of H, S, and V are following:

- **Hue**: The value of dominant color
- **Saturation**: The value of how much white mixes
- **Value**: The value of how much black mixes

In accordance with the test environment conditions, the most suitable H, S, V threshold values for our application were determined as in Table 7 on the following page:

	Lower Value	Upper Value
H	20	160
S	100	255
V	200	255

Table 7: HSV Values

After successfully creating the color mask and filter using the HSV values, the laser beam is completely separated into another video frame segment. Next, the boundaries of the laser beam are encircled by a white circle. Finally, the center of this white circle is marked with a green marker, which is also the center of the laser beam.

2.3.5 Drone Control

The DJI Tello has an onboard camera capable of shooting and streaming 720p video. Video image quality is often not the primary criterion when practicing real-time computer vision applications. For example, higher Frames Per Second (FPS) can be achieved by lowering the video resolution. In this regard, the high-resolution video stream from Tello is taken and downscaled into a video with a lower frame size, 640x480 pixels. Knowing the frame size is necessary for detecting the positions of green and red markers in the video image frame, as well as calculating the pointing error and sending the control command to the drone to correct the misalignment.

The response of the drone to the commands is a decisive criterion in the successful execution of control commands. In some cases, it is difficult to compensate for the pointing error in the fastest and most accurate way. Tello is capable of flying to a location at a minimum precision of 20 cm. When the “fly to a location” command is issued, it determines its speed according to the distance and flies to that location. Momentum is a property of all moving objects, and it can be calculated by multiplying the mass of the object by its velocity. Hence, the more momentum the drone has, the harder it is to stop. As a result, the drone sometimes fails to navigate to the desired location when flying to a point to tolerate misalignment.

Instead of flying to the calculated location directly, applying a Proportional, Integral and Derivative (PID) controlling technique may result in more sensitive and reliable results. PID stands for proportional integral derivative and attempts to fix the error by calculating the difference between measured and desired output. In order to implement PID control, proportional, integral, and derivative components must be defined. These parameters help in the stabilization of the drone [51]. P, I, D parameters, which were optimized by trial-and-error method during the development of the software and gave the most efficient result, are as in Table 8:

	x-axis	y-axis	z-axis
K_P	0.25	0.1	0.1
K_I	0.27	0.1	0.1
K_D	0.005	0	0.0035

Table 8: PID Parameters

After defining the PID parameters, they are integrated into the active tracking software. As a result of previous steps, a powerful computer as a ground station is used for controlling the drone. While the drone hovers, the video of the receive side is transferred to the ground station in real-time using the Wi-Fi connection. The video is processed based on Haar feature-based cascade classification at the ground station. Control commands are then sent to the drone to adjust its position for maintaining the FSO link.

2.4 Experimental Setup

In our experimental study, we employ a DJI Tello quadcopter, as illustrated in Figure 8 on page 20. Along with this small-sized quadcopter, a place holder is manufactured using a 3D printer to place the laser transmitter. This part is placed in the middle of the drone by being fixed from the notches on the side of the drone's body frame to prevent any wobble while the drone is hovering. Later, a mini red laser module with 5 mW and 650 nm optical wavelength is placed into the 3D printed holder. Although the laser is a snug fit in its place on the holder, it has been made adjustable with a 3 mm setscrew to minimize the error that may arise because of the manufacturing tolerance. Figure 9 depicts the transmitter side, which includes Tello, a 3D printed holder, and a laser module.

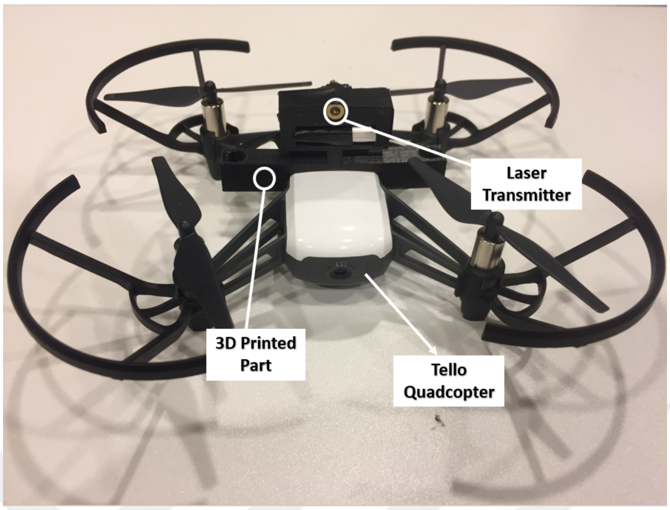

Figure 9: Transmitter Side

To measure the received power, a power meter (Si Photodiode type, S121C) by Thorlabs is used. A plano-convex lens (LA1145-B, Thorlabs) is employed before the power sensor for collimation purposes. This lens has a diameter of D_{Rx} = 50.8 mm and a focal length of f = 75 mm. The power sensor is placed right behind the receiver lens in a way that the active area of the sensor is aligned at the focal point of the lens, which is 75 mm. The specifications of the link setup are summarized in Table 9 on the following page. Furthermore, there is a computer as a ground station in the experimental setup where the computer vision is processed, and the drone is controlled.

The schematic of our experimental setup is presented in Figure 10 on the next page. The drone hovers at the height of 2 m above the ground. The link is in a horizontal direction, and the receiver is placed at the same height above the ground at a distance of L from the drone. As illustrated in Figure 10 on the following page, the onboard camera of the drone faces towards the receiver side (see blue shaded area). It transmits video to the ground station in real-time using the Wi-Fi connection. Then, the video is processed at the ground station based on Haar feature-based cascade classification. Based on the output of video processing, the control commands are generated by the

	Parameters	Values
Transmitter	Wavelength	650 *nm*
	Maximum optical power	3.5 *mW*
	Beam Divergence	38 *mrad*
	Aperture size	4.5 *mm*
Receiver	Detector type	Si Photodiode
	Wavelength range	400-1100 *nm*
	Power range	500 *nW* – 500 *mW*
	Lens aperture size	$D_{Rx} = 50.8\ mm$
	Lens focal length	f=75 *mm*
	PD responsivity R	3.74 *mA/W*
	Resolution	10 *nW*

Table 9: Specifications of the link setup

ground station using the computed distances and orientations. Afterward, the drone maintains its direction and position towards the required point to ensure the active link connection.

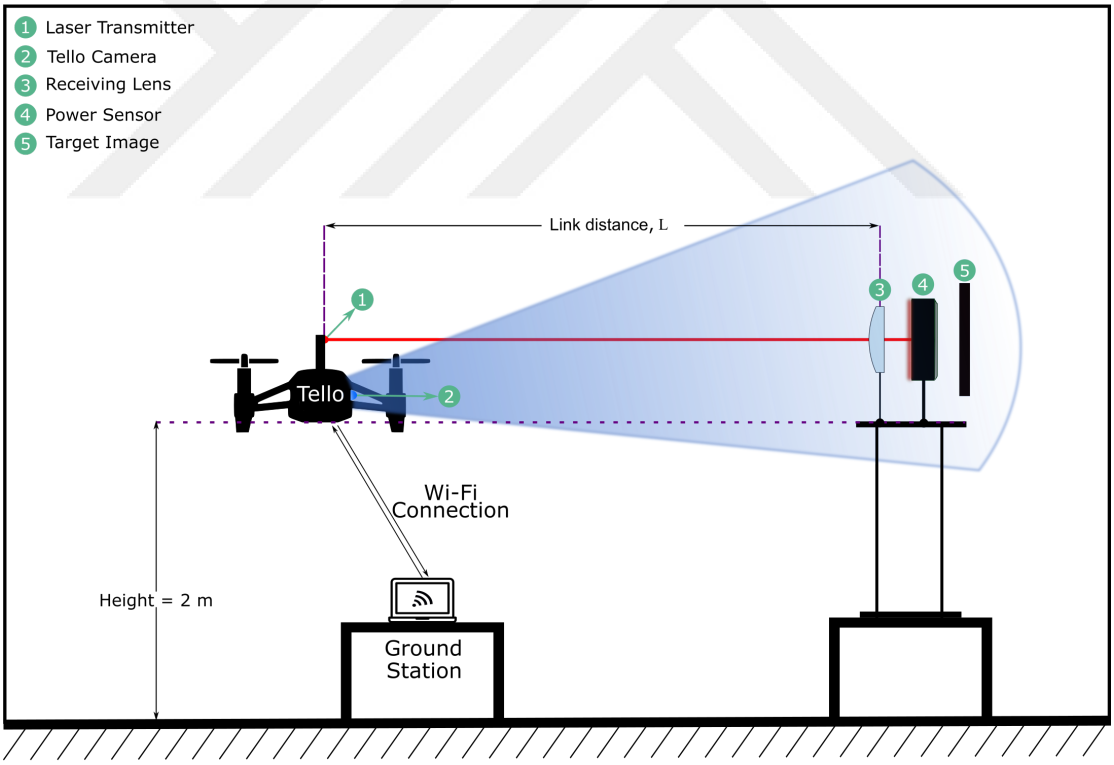

Figure 10: The schematic of the quadcopter experiment setup

2.5 *Experiment Results*

FSO communication system commonly comprises a laser source, optic equipment (e.g., lens, filter), and electro-optic electronics. Each of these components causes performance loss in different ways by their nature. Minimizing these losses and trying to improve performance is an engineering effort. First of all, we start by analyzing the shape of the transmitted laser beam. The original beam shape of the employed low-cost laser is depicted Figure 11(a). In an effort to have a beam shape with better quality and match with analytical results available in the literature, we create a near-Gaussian beam profile (see Figure 11(b)) by engineering the collimating lens of the laser and using 3D printed pinhole adjacent to the output of the laser beam.

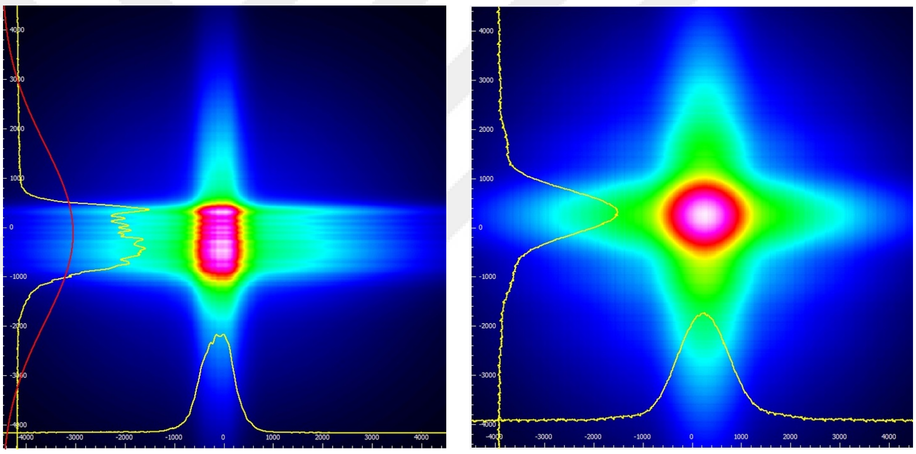

(a) (b)

Figure 11: Beam shape profile of the laser at the receiver: a) Original and b) Engineered

The most important performance criterion in an FSO system is the power of the received signal. In order to verify the experimental setup, we make a power measurement for a fixed point-to-point case. Under the controlled laboratory environment, excluding the atmospheric and optical losses and having only geometrical loss, the received power, P_r is given by [52]

$$P_r = P_t \frac{D_{R_x}^2}{(D_{T_x} + \theta L)^2} \tag{2.1}$$

The losses caused by the divergence of the optical beam are referred to as geometrical losses. A free-space optical system is often designed with the laser beam diverging along the way from the transmitter to the receiver. In order to calculate the geometrical loss, the divergence angle of the transmitted beam is required. For this purpose, the beam wavefront is placed 250 mm apart, and the beam width at each distance is recorded. For calculating the divergence angle, the equation is

$$\theta = 2\tan^{-1}\left(\frac{r_2 - r_1}{d}\right), \tag{2.2}$$

where d = 250 mm and r_1=11.75 mm, r_2=16.5 mm are the beam radius at position 1 and 2. The beam divergence has been found to be θ=38 $mrad$. The large value of divergence angle is intentionally adjusted to mimic possible implementation in which the received beam diameter is much greater than the aperture in regards to collecting more power. For a transmit power of P_t=3.5 mW, (2.1) gives received power values as P_r= 1.4, 0.73, 0.42 mW for L = 2, 3, and 4 m, respectively. Before installing the laser transmitter on the drone, we measure the received power. The measurements yield 1.38, 0.64, and 0.36 mW for L = 2, 3, and 4 m, respectively, confirming the accuracy of our setup. The small differences between measured and analytical results are due to power sensor efficiency and non-perfect Gaussian beam shape. These measured values for the fixed case can also serve as an upper bound for the later measurements.

In our measurement campaign, we record the power values at the receiver while the drone is in the hovering state. In order to minimize the effect of noise on the measurements, we use a high sampling rate of 220 $samples/sec$. Although this is much faster than the displacements, a higher number of samples reduces the noise significantly. To acquire a sufficient amount of samples for averaging purposes, we record the signal over 7-8 minutes. The samples are divided into smaller blocks of 44 samples per block and averaged to further reduce noise effects. The acquired samples are processed offline in MATLAB.

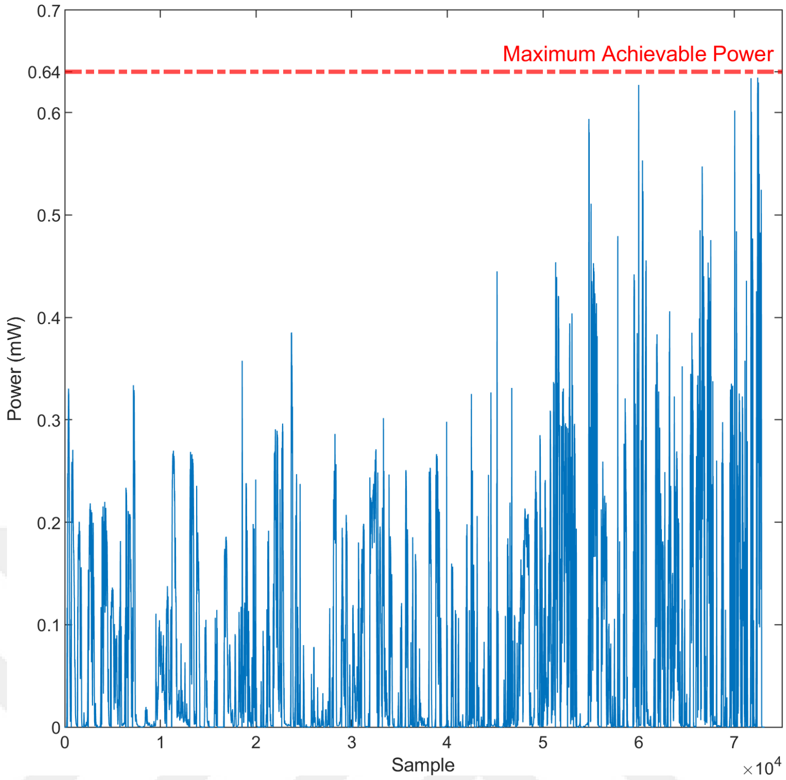

(a) without tracking

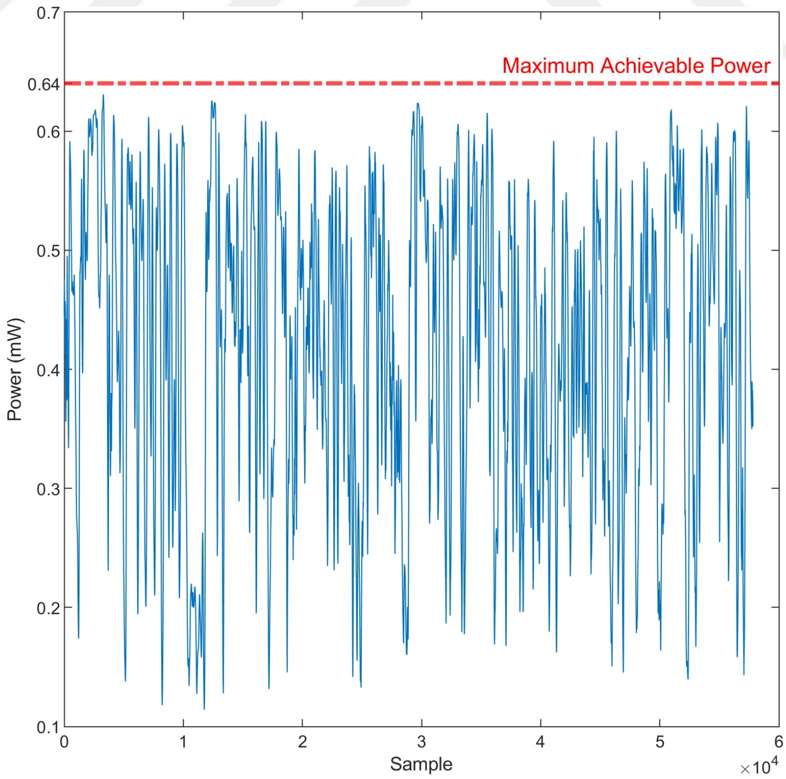

(b) with tracking

Figure 12: Received power at $L = 3\ m$

We perform our measurements at three different distances ($L = 2$, 3, and 4 m) with and without the tracking system. As an example, one instance of the measured received powers is depicted in Figure 12 on the previous page for $L = 3$ m. The received power value of 0.64 mW measured for the fixed case is provided as a benchmark (see red dashed lines). From the figures, it is observed that received power exhibits severe fluctuations. Displacements in the X and Y axes result in these power fluctuations, effectively resulting in a fading effect [34–37]. From the comparison of Figure 12(a) on the preceding page (without tracking) and Figure 12(b) on the previous page (with tracking), it can be readily checked that the tracking system has two benefits. First, it helps to keep the link active. Unlike the non-tracking system in Figure 12(a) on the preceding page, where link interruptions are observed (i.e., received power becomes zero at some instances), it can be observed that link interruptions do not take place (i.e., received power is always non-zero) for the tracking system as observed in Figure 12(b) on the previous page. Second, tracking helps to achieve higher values of received power on average since the effect of pointing error induced fading is mitigated to some extent through the tracking mechanism.

We plot the histogram of the received powers for all three distances under consideration in Figure 13 on the following page Maximum achievable power for each distance (i.e., measured for fixed deployment) is also included. It can be observed that the histogram for the system without tracking is in the form of a decreasing function. In other words, it is more likely to receive less power in most instances. This is expected since the pointing error induced fading will exhibit larger variance and induce larger attenuations. When we turn on our tracking system and repeat the experiment, it is observed that the histogram is in the form of an increasing function, and it is more likely to receive higher levels of power. This is as a result of the fact that tracking helps to reduce the variance of pointing error induced fading. Therefore, the performance is significantly enhanced in comparison to the non-tracking system.

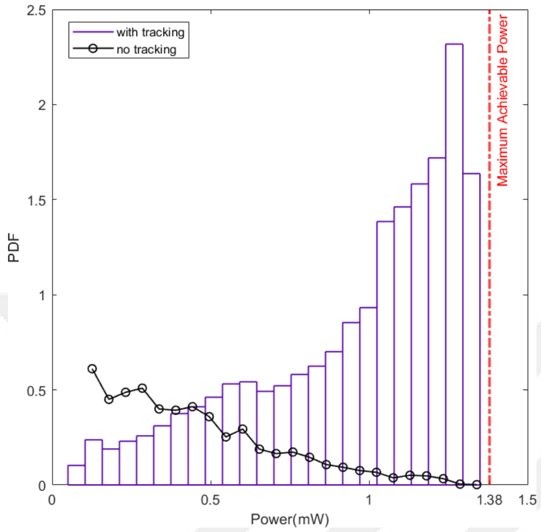

(a) The histogram of received power for $L = 2\ m$

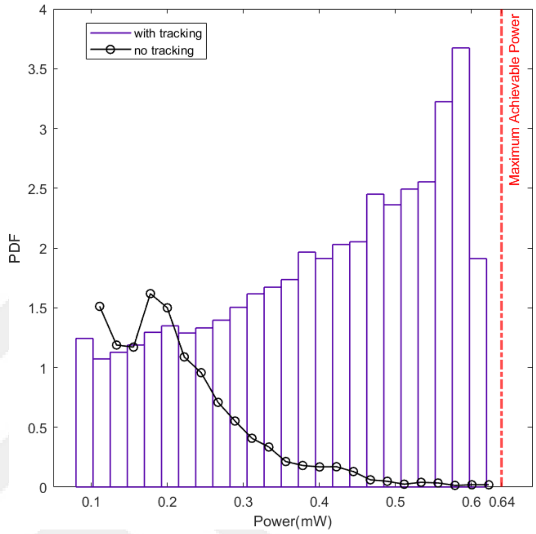

(b) The histogram of received power for $L = 3\ m$

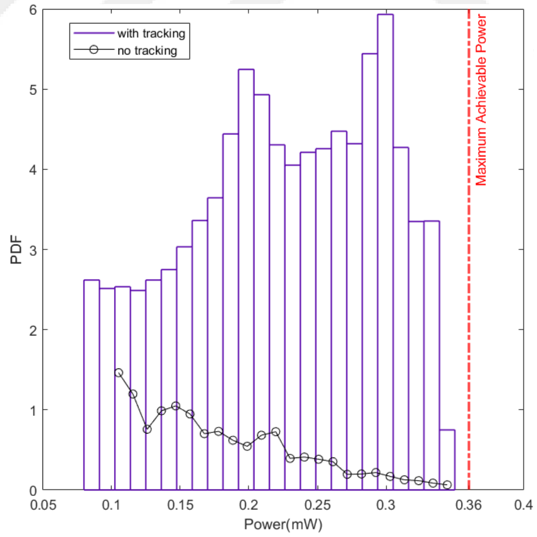

(c) The histogram of received power for $L = 4\ m$

Figure 13: The histogram of received powers

CHAPTER III

MEMS SCANNER EXPERIMENT

3.1 MEMS Scanning Technology

Microelectromechanical systems technology, which involves the microscale integration of mechanical and electrical components using microfabrication processes, is well-known and has already had a serious impact on many engineering and research fields. Laser projectors, 3D printers, and fiberoptic communications have all benefited greatly from MEMS technology. There have also been several advancements in the use of MEMS laser scanners for autonomous driving, robotics, virtual reality/augmented reality. MEMS mirrors can deflect a laser beam both statically and dynamically. For example, a MEMS mirror can remain very robust and precise at an angle when focusing a beam to a certain point, or it can be steered dynamically to track an object very fast [53].

While determining a suitable MEMS device for an application to be used, criteria such as operating frequency, mirror size, mode (i.e., static, dynamic) are considered. According to the actuation principles, MEMS scanners can be examined in 4 main categories as in Table 10.

Actuation	**Parameter**
Electrostatic (ESA)	displacement
Electromagnetic (EMA)	displacement
Piezoelectric (PEA)	force
Electrothermal (ETA)	strain

Table 10: Actuation principles of MEMS scanners

Electrostatic actuators are the most widely used actuation in MEMS devices due to their easy integration and the use of conventional materials. The electrostatic attraction between two plates generates the electrostatic force, and this force is used to actuate the MEMS device. Piezoelectric actuation requires advanced fabrication and machinery due to the utilization of unusual materials such as Zinc Oxide (ZnO), Aluminum Nitride (AlN), Lead Zirconate Titanate (PZT), etc. Therefore, this can be a disadvantage when compared to Electrostatic (ESA). Applying voltage bias on piezoelectric substrate results in deformation, which is a displacement change in the nanometer range. The Electromagnetic (EMA) scheme is actuated under the influence of magnetic fields generated by coils and magnets. Comparing to ESA, a larger actuation force can be created in EMA, but it is a drawback against others by size. Another method is to use the thermal effect as an actuator. The Joule effect is a common method of increasing temperature by passing a high current through a conducting material. As a result of the deformation as in Piezoelectric (PEA) caused by temperature change, thermal actuation takes place [54].

As another characterizing element among MEMS mirrors, the operating modes are classified in two ways:

- Resonant Mode (non-linear mode)
- Non-resonant Mode (linear mode)

Resonant mode is a non-linear operation mode that is driven at the resonant frequency of the mirror. Although the high-speed operation is feasible, the optical deflection angle of the mirror cannot be precisely managed. On the contrary, the angle of the MEMS mirror can be operated precisely in non-resonant mode with the benefits of linearity. Such mirrors are operated in lower frequencies than the natural frequency of the MEMS mirror to avoid resonance [55].

Optical beam steering can be achieved by Two-dimensional (2D) scanning. For a 2D scan, each rotational axis must be operated with one of the operating modes. The bi-resonant operating modes yield a Lissajous pattern, where point-to-point scanning mode happens when both axes are in non-resonant mode. In order to take advantage of both modes, modern 2D MEMS mirror applications have a configuration called raster scanning, in which low frequency non-resonant mode and high frequency resonant mode are paired together. [56]

3.2 Computer Simulation

As stated in the previous Chapter 2 on page 12, IMU sensors are used in drones for navigation, stabilization, and control purposes. Thanks to the included gyroscope sensor, the angular orientation of a drone can be obtained. In addition, the acceleration measurements from the IMU sensor can be read for all 3 axes. Double integration of the acceleration estimates the position of the sensor. This calculation alone is not enough because the gravity must be included in the calculation with respect to the drone's orientation. Dead-reckoning is the process of combining readings from IMU sensors to derive the position of a drone. While it is theoretically possible to accurately determine the position of the drone with the best sensors and signal processing, in practice, this is not easy to achieve. The constant accumulation of errors in the sensor, which is mentioned in Chapter 2 on page 12, and also causes misalignment, is caused by the double integration of the biased sensor readings. As a result, the data obtained from IMU and calculated using the dead-reckoning process is not reliable.

Computer simulations are used in the engineering discipline when investigating unknown and complex real-world problems or developing new applications. Physical experiments require models on a larger scale than computer simulations and are not practical in terms of time and cost. Thus, the number of trials and errors that can be executed in simulations is quite feasible when compared to real tests.

Computer simulations play an important role in the field of robotics. Many important design steps, from kinematic and dynamic analysis to control algorithms, are developed through computer simulations. One of the leading simulation tools in the field of robotics is Robot Operating System. ROS offers an excellent software interface to inspect and interact with simulation models. Known as the meta operating system, ROS is run along with an operating system such as Windows, Linux, or Mac and establishes a communication interface between computer operating systems and users. C++ and Python scripts can be executed directly to simulate applications in ROS, which makes it very practical to manipulate a robot design. Another feature and benefit of selecting ROS as a simulation environment, subsystems such as sensors and cameras, can also be integrated into the simulation. As an open-source robotic software system, many robots, sensors, and add-on libraries are available free of charge.

One of the indispensable toolboxes in robot simulations is Gazebo, a complement to ROS. Serving as a 3D simulator, it is possible to create a physical environment with dynamics (i.e., gravity, inertia) by Gazebo's multiple physics engines. Gazebo is very efficient at implementing sensors. Noises must be taken into account while analyzing sensor data. As a matter of fact, reaching data without noise is impossible in the real world. The ideal robot design should be substantiated by ensuring that the simulation environment produces noisy data like in the real world. Thanks to the sensor plugins of the Gazebo, it is possible to generate noisy data. Because of all these features and ROS integration, Gazebo simulation has become the most preferred simulation program by roboticists.

Robot models are represented in the Unified Robotic Description Format (URDF) files in ROS. All components, kinematic and dynamic properties are specified in the URDF file using Extensible Markup Language (XML) syntax. Even though Gazebo uses the Simulation Description Format (SDF) files natively, URDF files can be converted to SDF files in order to work properly with Gazebo. The DJI Tello URDF model is available in open source, and we use it in our Gazebo simulation [57].

3.3 Experimental Setup

In this study, unlike our previous experiment, we use a MEMS scanner by Mirrorcle, which allows us to deflect the laser beam emitted from a fixed laser source in the direction we want, instead of a moving transmitter such as a drone. This MEMS Scanner enables extremely quick optical beam steering in two axes while consuming very little power. In point-to-point or quasi-static mode, the mirrors divert laser beams to scanning angles of up to 32° on each axis and larger angles in a non-linear mode. The mirror surfaces are covered with a thin layer of metal with strong reflectivity. The monolithic single-crystal silicon used in the device delivers maximum reliability and repeatability. The mechanical tilt precision of the actuator is no less than 14 bits (16,384 places) on each axis. This tilt resolution is within 0.6 milli-degrees or 10 micro-radians for most devices having a mechanical tilt range of -5° to +5° on each axis [58].

The study starts off by placing our components on solid aluminum optical breadboards. At the transmitter side, there is a temperature-controlled laser diode mount (TCLDM9) by Thorlabs and a visible high power laser diode with high output power, 35 *mW* and 690 *nm* optical wavelength. We create a near-Gaussian beam profile (see Figure 15(b) on page 38) by placing two distinct pinholes after the laser mount in order to have a better beamshape that matches analytical results. After that, an aspheric lens is put in front of the second pinhole with the purpose of focusing the beam so that the MEMS mirror's center is at the focal point of the lens. Accordingly, the MEMS mirror is placed at the point where the laser is focused.

To measure the received power, a power meter (Si Photodiode type, S121C) by Thorlabs is used. A plano-convex lens (LA1145-B, Thorlabs) is employed before the power sensor for collimation purposes. This lens has a diameter of D_{Rx} = 50.8 mm and a focal length of f = 75 mm. The power sensor is placed right behind the receiver lens in a way that the active area of the sensor is aligned at the focal point of the lens, which is 75 mm.

The specifications of the link setup are summarized in Table 11 on the next page

3.4 Experimental Results

In this section, we explain our experimental setup and emulate a hovering drone using a MEMS scanner and analyze the statistics of the hovering drone and also the probability distribution for the intensity of the received signal. First, the MEMS scanner emulates zero-mean independent Gaussian random variables for the x and y axes to investigate

	Parameters	Values
Transmitter	Wavelength	690 *nm*
	Maximum optical power	21.75 *mW*
	Beam Divergence	38 *mrad*
	Aperture size	4.5 *mm*
Receiver	Detector type	Si Photodiode
	Wavelength range	400-1100 *nm*
	Power range	500 *nW* – 500 *mW*
	Lens aperture size	$D_{Rx} = 50.8\ mm$
	Lens focal length	f=75 *mm*
	PD responsivity R	3.74 *mA/W*
	Resolution	10 *nW*

Table 11: Specifications of the MEMS Scanner link setup

the works in literature. After that, we emulate the MEMS mirror based on the data from computer simulations.

3.4.1 Pointing Error Loss

The pointing error is the primary problem of FSO communication as briefly mentioned in Section 2.5 on page 25 and Section 1.4 on page 9. Assuming no external effect, pointing error is usually caused by installation error where the propagation axis of the beam does not coincide with the center of the receiver. Another possibility is that the FSO link has a tracking mechanism with persistent errors that might cause a pointing error. In an ideal scenario where the laser beam does not exceed the receiving aperture and reliable communication is achieved, the problem with drone-based FSO communication systems is closer to the second option.

Examining the beam shape geometrics of the transmitting laser is critical for the analysis of pointing error statistics. From the review of pointing error in the literature, only the ideal Gaussian beamshape is deemed [34–38,59,60]. Therefore, in Section 3.3 on page 33, we adjusted our beamshape,15(b), correspondingly. Under the assumption of Gaussian beam profile, the normalized intensity profile at the receiver at a distance Z, is given by [61]

$$I_r(r,Z) = \frac{2}{\pi w_z} \exp\left(-\frac{2\left(x^2+y^2\right)}{w_z^2}\right), \tag{3.1}$$

where $r = [x, y]$ is the distance vector from the beam center, w_z is the beam waist at distance Z. Assuming the misalignment r_d occured and the beam shifted to the new position at the receiver plane such as $r_d = [x_d\ , y_d]$. The new location of the beam center with respect to initial position can be obtained as

$$x_d = x_r + Z\tan(\theta_x), \text{ and } y_d = y_r + Z\tan(\theta_y). \tag{3.2}$$

Considering small-angle approximation in terms of θ_x and θ_y, (3.2) is simplified as follow

$$x_d = x_r + Z\theta_x, \text{ and } y_d = y_r + Z\theta_y, \tag{3.3}$$

where x_r, y_r, θ_x, and θ_y are zero-mean Gaussian random variables with variance $2\sigma_r^2$ and σ_θ^2, respectively. Following the derivations from [38, Eqn.(10)], the pointing error, h_p can be approximated as

$$h_p \simeq A_0 \exp\left(-2r_d^2/w_{z_{\text{eq}}}^2\right). \tag{3.4}$$

where $r_d = \sqrt{x_d^2 + y_d^2}$, $A_0 = (\text{erf}(\nu))^2$, $\nu = \frac{\sqrt{\pi} r_x}{\sqrt{2} w_z}$ and $w_{z_{\text{eq}}}^2 = w_z^2 \frac{\sqrt{\pi}\,\text{erf}(\nu)}{2\nu \exp(-\nu^2)}$. Since $x_d \sim \mathcal{N}\left(\theta_x Z, 2\sigma_r^2\right)$ and $y_d \sim \mathcal{N}\left(\theta_y Z, 2\sigma_r^2\right)$ have a Gaussian distribution, r_d conditioned on θ_x, and θ_y has a Rician distribution.

3.4.2 Measurement Campaign

In this section, we emulate the drone-based FSO link using a MEMS scanner. We take measurements using a power meter with a high sampling rate and analyze the statistics of the hovering drone and also the probability distribution for the intensity of the received power. The schematic of our experimental setup is presented in Figure 14 on the next page. The beamshape characteristics of the laser are analyzed using the same beam profiler as in Chapter 2 on page 12. The original beamshape of the laser diode is depicted in Figure 15(a) on page 38. The derived PDF of h_p in Equation (3.4) is under the assumption of Gaussian beam profile. Therefore, we create a Gaussian beam profile by adjusting two adjacent pinholes to in front of the laser source. Hypothetically, when the aperture diameter of the pinhole tends to zero the beam profile, it converges to a

Gaussian distribution as it is depicted in Figure 15(a) on the next page. However, it is worth noting that this is impractical for an FSO system from an energy delivering point of view since the pinhole reduces the output power. On the other hand, having a highly powerful laser source, 35 mW, in our experiment, this is out of our interest. Further, the intensity profile of the laser beam is mapped to cartesian coordinates of the x-axis and y-axis, and then Gaussian distribution is fitted as it is shown in Figure 16 on the following page.

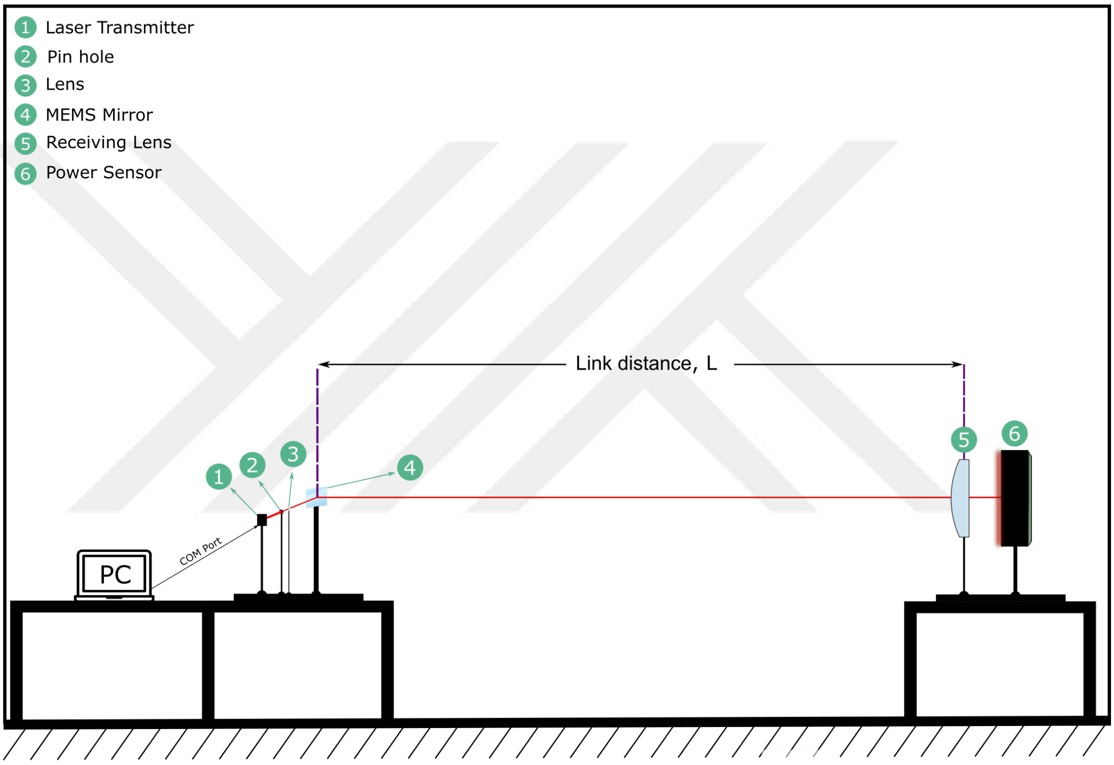

Figure 14: The schematic of the MEMS experiment setup

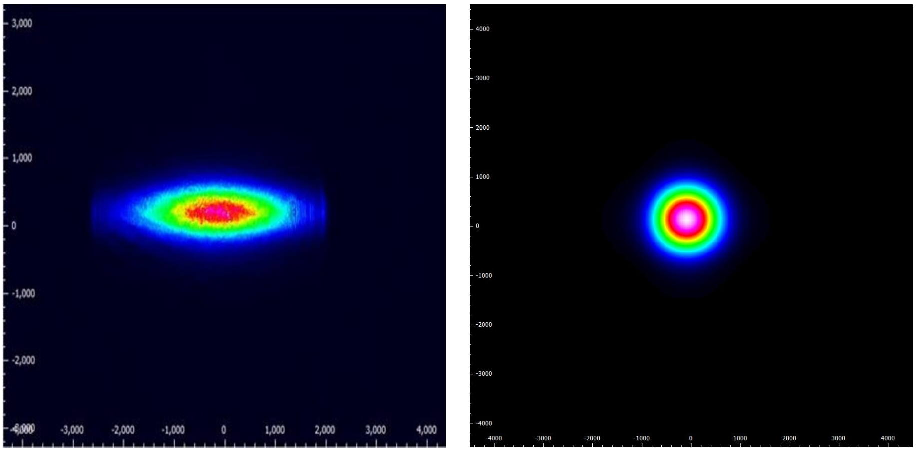

(a) (b)

Figure 15: Beam shape profile of the laser at the receiver: a) Original and b) Engineered

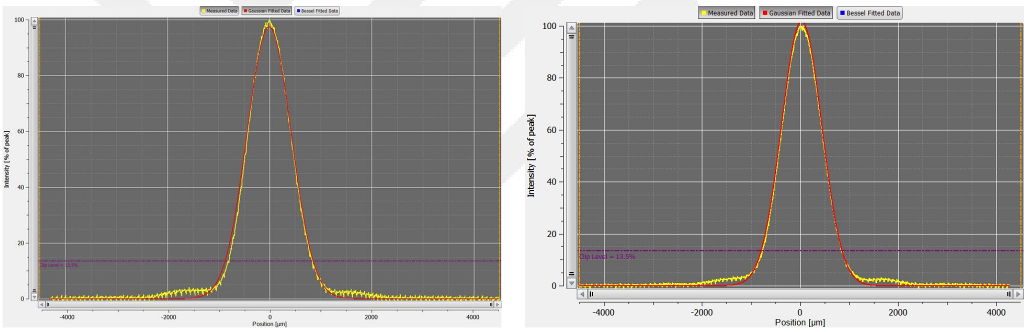

(a) (b)

Figure 16: The intensity profile in cartesian coordinates of a) x-axis and b) y-axis

As in Section 2.5 on page 25, we use 2.2 to calculate beam divergence angle and then calculate P_r, using 2.1 for L = 3 m. The received power value of 2.6647 mW measured for the fixed case is provided as a maximum achievable power in Figure 23 on page 44 (see red dashed lines).

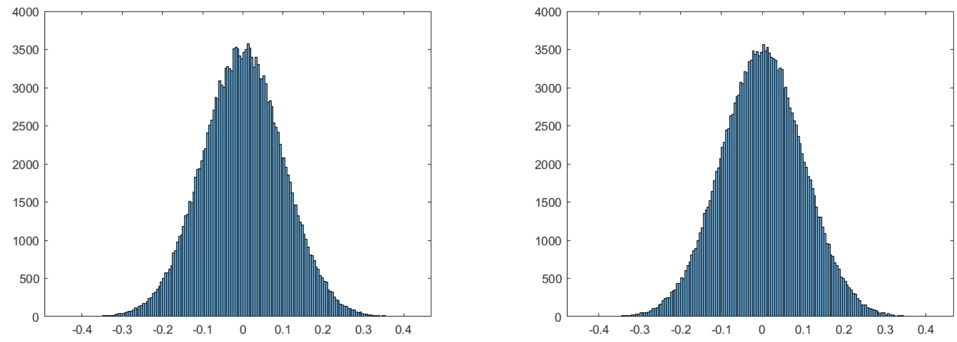

(a) PDF of the x-axis

(b) PDF of the y-axis

Figure 17: Probability density function of the MATLAB generated data a) x-axis and b) y-axis

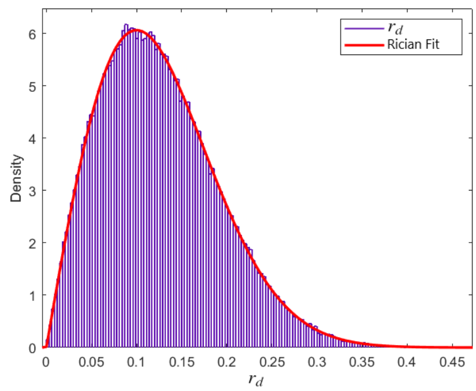

Figure 18: Probability density function of the MATLAB generated r_d data

Another beam specification, w_z, which is also a parameter of h_p in 3.4, is calculated as follows

$$w_L = \left(D_{tx} + \tan\left(\theta\right) L\right)/2 \tag{3.5}$$

In the first stage of the experiment, the MEMS mirror emulates the data we generate via MATLAB such that x and y axes are zero-mean independent Gaussian random variables to verify the h_p in 3.4. Figure 17 depicts the PDF of the x and y. Using 3.4, we then plot the PDF of the r_d, as seen in Figure 18.

To reduce the effect of electro-optical conversion constants, we deal with the normalized intensity power as in Equation (3.1) on page 35. In order to catch the sampling rate of the MEMS scanner on the measurements, we prefer to use a sampling rate of 10 Sa/sec. To acquire a sufficient amount of samples, we record the intensity change on the power meter caused by the pointing error over 30 minutes. The acquired samples are processed offline in MATLAB. The noise of the signal is significantly reduced and the normalized intensity versus time which shows the attenuations caused by pointing error is depicted in Figure 19. As the normalization applied, this manifest itself as pointing error channel coefficient changing through time. This data is used to extract the probability density function of optical received intensity. Finally, in Figure 20 on the next page, we plot the Probability Density Function (PDF) of the pointing error, h_p and compare it against the theoretical formula in Equation (3.4) on page 36.

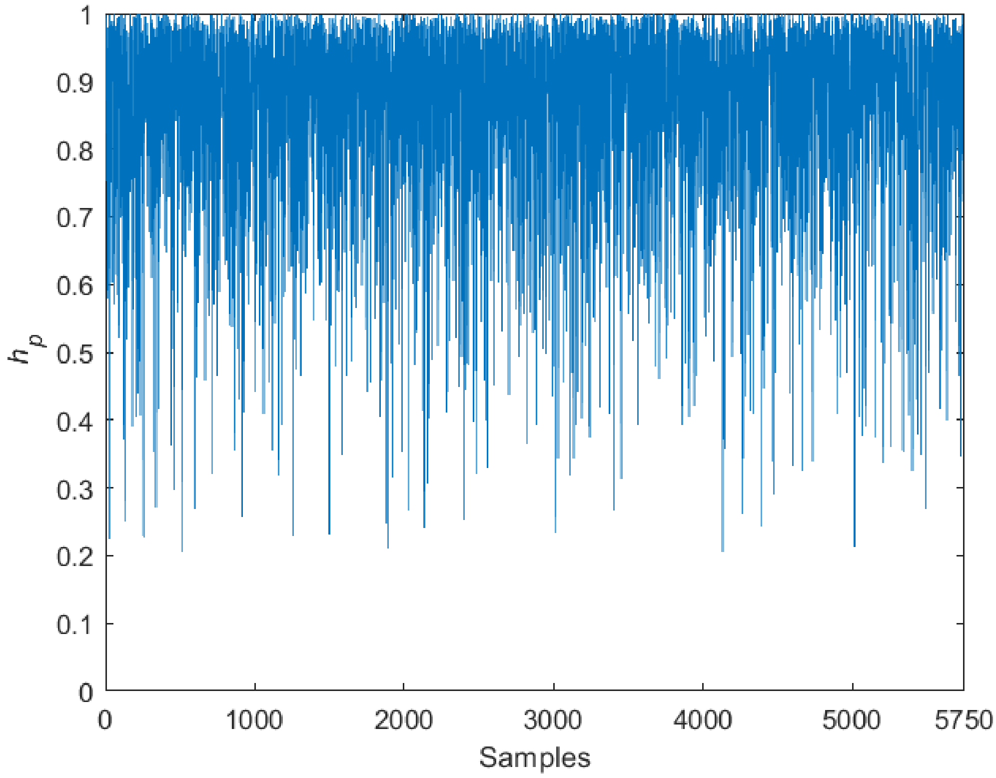

Figure 19: Pointing error versus time

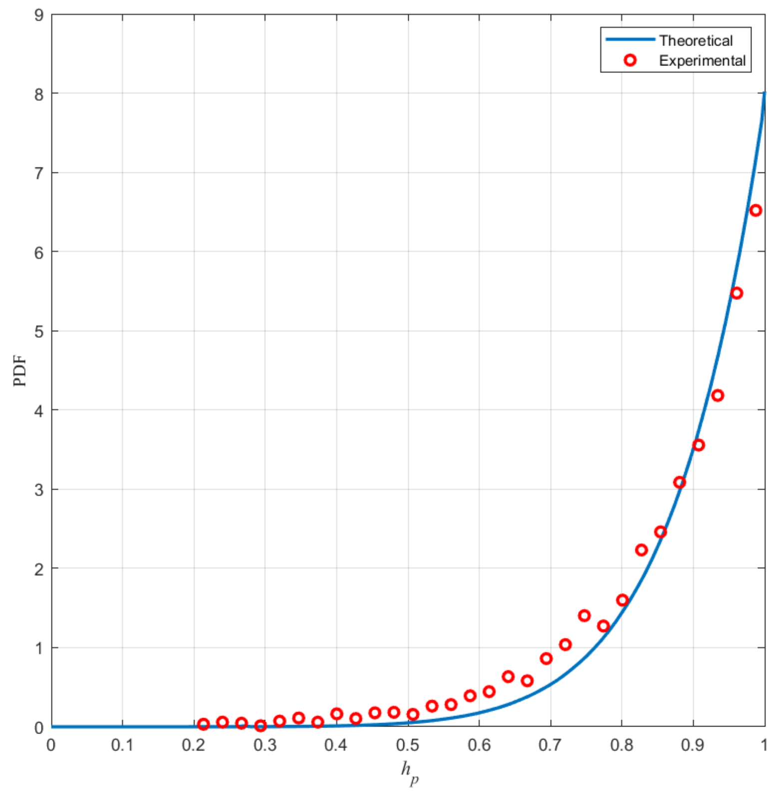

Figure 20: Probability density function of h_p theoretical vs. experimental

It can be observed from Figure 20 that experimental results are in trend to agree with the theoretical expression in h_p in 3.4. Results also confirms the reliability of the pointing error under near-Gaussian beam profile and zero-mean independent Gaussian random variables in horizontal and elevation displacement. In order to close the difference between two results, we need a longer run test of more than 30 minutes and have an ideal Gaussian beam profile.

After a successful theory benchmark, we emulate the drone data from the computer simulation, ROS and Gazebo, where the sensor errors also have an impact. This part of the experiment aims to compare the results of our experiment with a real drone in Chapter 2 on page 12. When the data samples taken from the computer simulation are examined, it is seen that the hovering drone movement in both axes is different from each other. This is because the accumulation of the state errors of the vision sensor used in the elevation control on the system is different from the IMU sensor in charge of the control on the horizontal axis. Figure 21 on the next page depicts the PDF of the x and y axes of the drone simulation from the ROS. Using 3.4, we then plot the PDF of the r_d, as seen in Figure 22 on the following page. As explained in Section 3.4.1 on page 35, the PDF of the r_d would be expected to be the Rician fit, but this would only be valid when both horizontal, and elevation displacements are zero-mean identical Gaussian random variables.

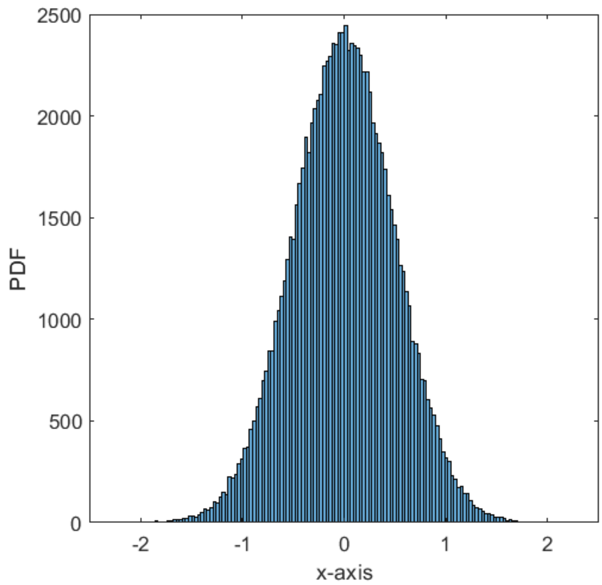

(a) Probability density function of x-axis

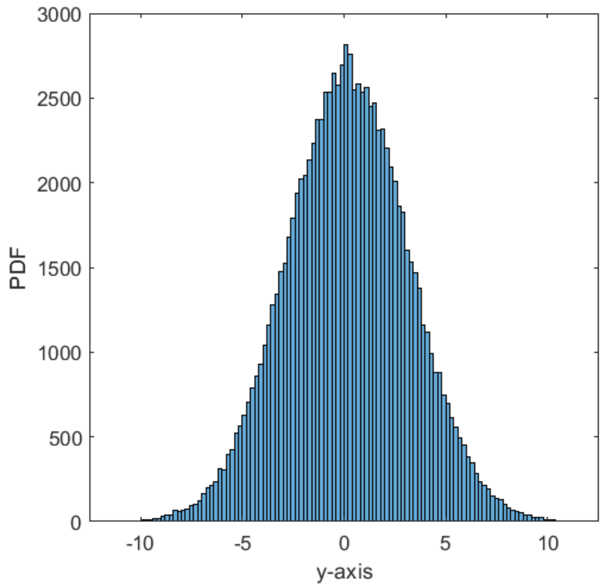

(b) Probability density function of y-axis

Figure 21: Probability density function of a) x-axis and b) y-axis

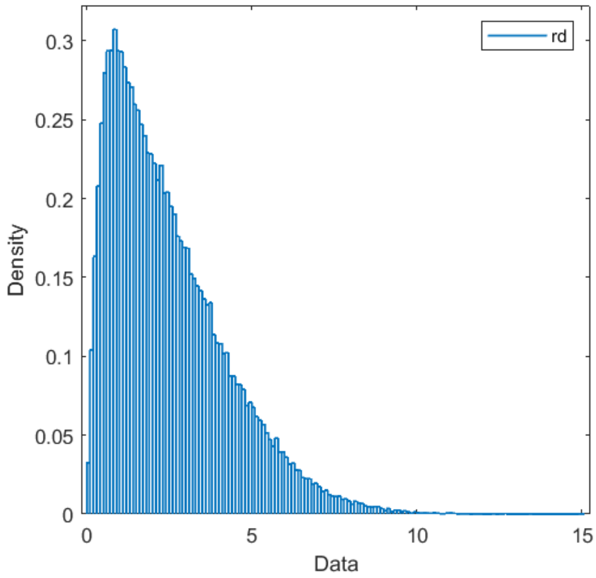

(a) PDF of the r_d without fit

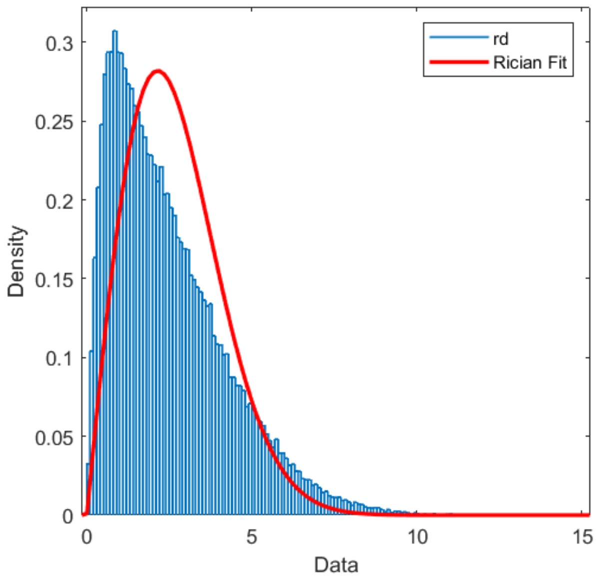

(b) PDF of the r_d with the Rician fit

Figure 22: The PDF of the r_d from computer simulation a) without fit and b) with the Rician fit

As in the previos experiment phase, where we emulate the generated data through the MATLAB, in order to catch the sampling rate of the MEMS scanner on the measurements, we prefer to use a sampling rate of 10 Sa/sec in this experiment as well. We collect the power measurements on the power meter caused by the pointing error over

30 minutes to acquire a sufficient amount of samples. We perform our measurements at $L = 3\ m$ and plot the histogram of the received powers as shown in Figure 23.

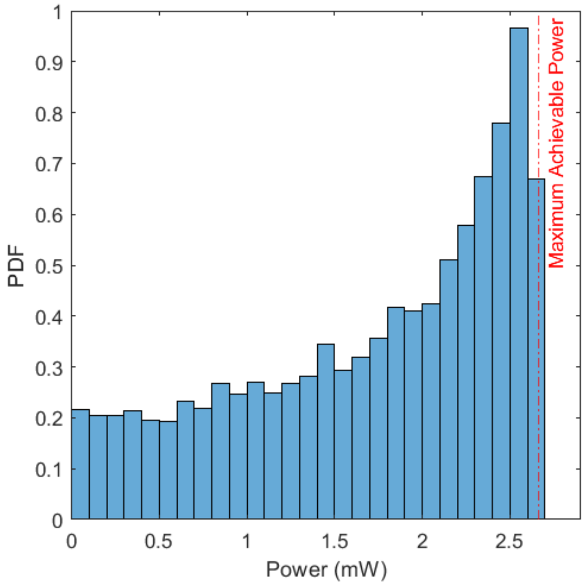

Figure 23: Probability density function of h_p in MEMS experiment

The Figure 23 shows that our results follow a very similar trend with our previous experiments in Figure 13 on page 29. Without further ado, drones are equipped with many different sensors in the real world. Like the DJI Tello we used in our experiment, the drone control can be provided from two non-identical sensors on two different axes. This causes error characteristics in the two axes to be distinct from each other. Apart from sensor errors, a wind speed vector will also have a different effect on the axes of the drone. Therefore, choosing zero-mean independent Gaussian random variables axes may not be the right approach.

CHAPTER IV

CONCLUSION

In this thesis, we carried out an experimental study to demonstrate the effect of pointing errors in drone-based FSO systems both using a real quadcopter, DJI Tello, and a MEMS Scanner. In our experimental set-up, although the drone has a positioning system, stabilization accuracy in the hovering state was not found sufficiently high for an acceptable FSO link alignment. In an effort to avoid link interruptions, we employed a tracking method based on a supervised learning method, namely Haar feature-based cascade classification. We performed an extensive measurement campaign and recorded power measurements for drone-based FSO systems. The received power exhibits severe fluctuations due to displacements of the transceiver, effectively resulting in a fading effect. Our results further demonstrated that the tracking system maximizes the received power, and pointing error is significantly reduced, providing a more stable connection. Moreover, as another measurement campaign, using a MEMS scanner, we investigated whether the studies in the literature match real-life situations. For this, we first created our own data on MATLAB and then took power measurements by driving the MEMS mirror, then we emulate drone data from computer simulations. Consequently, it was predicted that the measurements made were close to following the trend in the literature and would match better if the measurement was recorded for a longer time.

Bibliography

[1] Cisco, "Cisco annual internet report - cisco annual internet report (2018–2023) white paper," Mar 2020.

[2] Ericsson, "Ericsson mobility report november 2021," Nov 2021.

[3] Amakawa, S and Aslam, Z. and Buckwater, J. and Caputo, S. and Chaoub, A. and Chen, Y. and Corre, Y. and Fujishima, M. and Ganghua, Y. and Gao, S. and Grzyb, J. and Han, C. and JUe, G. and Kokkoniemi, J. and Lai, Z. and Li, Y. and Millhaem, M. and Moerman, Ingrid and Mucchi, L. and Myllymäki, S. and Nichols, R. and Ocket, I. and Robertson, M. and Rodwell, M., "White Paper on RF enabling 6G–opportunities and challenges from technology to spectrum," 2021.

[4] X. Ge, H. Cheng, M. Guizani, and T. Han, "5g wireless backhaul networks: challenges and research advances," *IEEE Network*, vol. 28, no. 6, pp. 6–11, 2014.

[5] O. Tipmongkolsilp, S. Zaghloul, and A. Jukan, "The evolution of cellular backhaul technologies: Current issues and future trends," *IEEE Communications Surveys Tutorials*, vol. 13, no. 1, pp. 97–113, 2011.

[6] S. Chia, M. Gasparroni, and P. Brick, "The next challenge for cellular networks: backhaul," *IEEE Microwave Magazine*, vol. 10, no. 5, pp. 54–66, 2009.

[7] F. Demers, H. Yanikomeroglu, and M. St-Hilaire, "A survey of opportunities for free space optics in next generation cellular networks," in *2011 Ninth Annual Communication Networks and Services Research Conference*, pp. 210–216, 2011.

[8] M. Alzenad, M. Z. Shakir, H. Yanikomeroglu, and M.-S. Alouini, "Fso-based vertical backhaul/fronthaul framework for 5g+ wireless networks," *IEEE Communications Magazine*, vol. 56, no. 1, pp. 218–224, 2018.

[9] Y. Li, M. Pióro, and V. Angelakisi, "Design of cellular backhaul topology using the fso technology," in *2013 2nd International Workshop on Optical Wireless Communications (IWOW)*, pp. 6–10, 2013.

[10] Y. Li, N. Pappas, V. Angelakis, M. Pióro, and D. Yuan, "Optimization of free space optical wireless network for cellular backhauling," *IEEE Journal on Selected Areas in Communications*, vol. 33, no. 9, pp. 1841–1854, 2015.

[11] M. Uysal and H. Nouri, "Optical wireless communications — an emerging technology," in *2014 16th International Conference on Transparent Optical Networks (ICTON)*, pp. 1–7, 2014.

[12] W. A. Cahyadi, Y. H. Chung, Z. Ghassemlooy, and N. B. Hassan, "Optical camera communications: Principles, modulations, potential and challenges," *Electronics*, vol. 9, p. 1339, Aug 2020.

[13] A. A. Huurdeman, *The worldwide history of Telecommunications*. J. Wiley, 2003.

[14] D. Begley, “”free-space laser communications: a historical perspective”,” in *The 15th Annual Meeting of the IEEE Lasers and Electro-Optics Society*, vol. 2, pp. 391–392 vol.2, 2002.

[15] J. Hecht 2, “Laser evolution,” 2009.

[16] M. A. Khalighi and M. Uysal, “Survey on free space optical communication: A communication theory perspective,” *IEEE Communications Surveys Tutorials*, vol. 16, no. 4, pp. 2231–2258, 2014.

[17] H. Kaushal and G. Kaddoum, “Optical communication in space: Challenges and mitigation techniques,” *IEEE Communications Surveys Tutorials*, vol. 19, no. 1, pp. 57–96, 2017.

[18] H. Haas, J. Elmirghani, and I. White, “Optical wireless communication,” *Philosophical Transactions of the Royal Society A: Mathematical, Physical and Engineering Sciences*, vol. 378, no. 2169, p. 20200051, 2020.

[19] D. Killinger, “Free space optics for laser communication through the air,” *Opt. Photon. News*, vol. 13, pp. 36–42, Oct 2002.

[20] H. González-Jorge, J. Martínez-Sánchez, M. Bueno, Arias, and Pedor, “Unmanned aerial systems for civil applications: A review,” *Drones*, vol. 1, p. 2, Jul 2017.

[21] B. Argrow, D. Lawrence, and E. Rasmussen, *UAV Systems for Sensor Dispersal, Telemetry, and Visualization in Hazardous Environments*.

[22] E. W. Frew and T. X. Brown, “Airborne communication networks for small unmanned aircraft systems,” *Proceedings of the IEEE*, vol. 96, no. 12, pp. 2008–2027, 2008.

[23] N. Elmeseiry, N. Alshaer, and T. Ismail, “A detailed survey and future directions of unmanned aerial vehicles (uavs) with potential applications,” *Aerospace*, vol. 8, no. 12, 2021.

[24] A. Fotouhi, H. Qiang, M. Ding, M. Hassan, L. G. Giordano, A. Garcia-Rodriguez, and J. Yuan, “Survey on uav cellular communications: Practical aspects, standardization advancements, regulation, and security challenges,” *IEEE Communications Surveys Tutorials*, vol. 21, no. 4, pp. 3417–3442, 2019.

[25] J. Hempel, “Inside facebook’s ambitious plan to connect the whole world,” Jan 2020.

[26] B. Moision, B. Erkmen, E. Keyes, T. Belt, O. Bowen, D. Brinkley, P. Csonka, M. Eglington, A. Kazmierski, N. hyong Kim, J. Moody, T. Tu, and W. Vermeer, “Demonstration of free-space optical communication for long-range data links between balloons on Project Loon,” in *Free-Space Laser Communication and Atmospheric Propagation XXIX* (H. Hemmati and D. M. Boroson, eds.), vol. 10096, pp. 259 – 272, International Society for Optics and Photonics, SPIE, 2017.

[27] F. Moll, J. Horwath, A. Shrestha, M. Brechtelsbauer, C. Fuchs, L. A. Martín Navajas, A. M. Lozano Souto, and D. Díaz González, “Demonstration of high-rate laser communications from a fast airborne platform,” *IEEE Journal on Selected Areas in Communications*, vol. 33, no. 9, pp. 1985–1995, 2015.

[28] M. Safari and M. Uysal, “Relay-assisted free-space optical communication,” *IEEE Transactions on Wireless Communications*, vol. 7, no. 12, pp. 5441–5449, 2008.

[29] W. Fawaz, C. Abou-Rjeily, and C. Assi, “Uav-aided cooperation for fso communication systems,” *IEEE Communications Magazine*, vol. 56, no. 1, pp. 70–75, 2018.

[30] M. Petkovic and M. Narandzic, “Overview of uav based free-space optical communication systems,” in *Interactive Collaborative Robotics* (A. Ronzhin, G. Rigoll, and R. Meshcheryakov, eds.), (Cham), pp. 270–277, Springer International Publishing, 2019.

[31] N. Letzepis and A. G. I. Fàbregas, *Hybrid RF/FSO communications*, p. 273–302. Cambridge University Press, 2012.

[32] S. Althunibat, O. S. Badarneh, R. Mesleh, and K. Qaraqe, “A hybrid free space optical-millimeter wave cooperative system,” *Optics Communications*, vol. 453, p. 124400, 2019.

[33] J. Ding, H. Mei, C.-L. I, H. Zhang, and W. Liu, “Frontier progress of unmanned aerial vehicles optical wireless technologies,” *Sensors*, vol. 20, no. 19, 2020.

[34] A. A. Farid and S. Hranilovic, “Outage capacity optimization for free-space optical links with pointing errors,” *Journal of Lightwave Technology*, vol. 25, no. 7, pp. 1702–1710, 2007.

[35] F. Yang, J. Cheng, and T. A. Tsiftsis, “Free-space optical communication with nonzero boresight pointing errors,” *IEEE Transactions on Communications*, vol. 62, no. 2, pp. 713–725, 2014.

[36] M. Najafi, H. Ajam, V. Jamali, P. D. Diamantoulakis, G. K. Karagiannidis, and R. Schober, “Statistical modeling of fso fronthaul channel for drone-based networks,” in *2018 IEEE International Conference on Communications (ICC)*, pp. 1–7, 2018.

[37] M. T. Dabiri, S. M. S. Sadough, and I. S. Ansari, “Tractable optical channel modeling between uavs,” *IEEE Transactions on Vehicular Technology*, vol. 68, no. 12, pp. 11543–11550, 2019.

[38] M. T. Dabiri, S. M. S. Sadough, and M. A. Khalighi, “Channel modeling and parameter optimization for hovering uav-based free-space optical links,” *IEEE Journal on Selected Areas in Communications*, vol. 36, no. 9, pp. 2104–2113, 2018.

[39] P. Viola and M. Jones, “Rapid object detection using a boosted cascade of simple features,” in *Proceedings of the 2001 IEEE Computer Society Conference on Computer Vision and Pattern Recognition. CVPR 2001*, vol. 1, pp. I–I, 2001.

[40] D. Tezza and M. Andujar, "The state-of-the-art of human–drone interaction: A survey," *IEEE Access*, vol. 7, pp. 167438–167454, 2019.

[41] G. Hoffmann, H. Huang, S. Waslander, and C. Tomlin, *Quadrotor Helicopter Flight Dynamics and Control: Theory and Experiment*.

[42] DJI, "User manual v1 - dji tello," Apr 2018.

[43] E. Ciobanu and N. Malczan, "What are gps drones, and why does it matter," Dec 2021.

[44] N. Barbour and G. Schmidt, "Inertial sensor technology trends," *IEEE Sensors Journal*, vol. 1, no. 4, pp. 332–339, 2001.

[45] Y. Kaymak, R. Rojas-Cessa, J. Feng, N. Ansari, M. Zhou, and T. Zhang, "A survey on acquisition, tracking, and pointing mechanisms for mobile free-space optical communications," *IEEE Communications Surveys Tutorials*, vol. 20, no. 2, pp. 1104–1123, 2018.

[46] G. Bradski, "The OpenCV Library," *Dr. Dobb's Journal of Software Tools*, 2000.

[47] J. Deng, W. Dong, R. Socher, L.-J. Li, K. Li, and L. Fei-Fei, "Imagenet: A large-scale hierarchical image database," in *2009 IEEE conference on computer vision and pattern recognition*, pp. 248–255, Ieee, 2009.

[48] R. Lienhart and J. Maydt, "An extended set of haar-like features for rapid object detection," in *Proceedings. International Conference on Image Processing*, vol. 1, pp. I–I, 2002.

[49] P. Carbonnelle, "Pypl popularity of programming language index," Dec 2021.

[50] G. Van Rossum and F. L. Drake, *Python 3 Reference Manual*. Scotts Valley, CA: CreateSpace, 2009.

[51] K. H. Ang, G. Chong, and Y. Li, "Pid control system analysis, design, and technology," *IEEE Transactions on Control Systems Technology*, vol. 13, no. 4, pp. 559–576, 2005.

[52] Z. Ghassemlooy, M. Uysal, M. A. Khalighi, V. Ribeiro, F. Moll, S. Zvanovec, and A. Belmonte, *An Overview of Optical Wireless Communications*, pp. 1–23. Cham: Springer International Publishing, 2016.

[53] H. Xie, "Editorial for the special issue on mems mirrors," *Micromachines*, vol. 9, no. 3, 2018.

[54] S. T. S. Holmström, U. Baran, and H. Urey, "Mems laser scanners: A review," *Journal of Microelectromechanical Systems*, vol. 23, no. 2, pp. 259–275, 2014.

[55] H. Urey, D. W. Wine, and T. D. Osborn, "Optical performance requirements for MEMS-scanner-based microdisplays," in *MOEMS and Miniaturized Systems* (M. E. Motamedi and R. Goering, eds.), vol. 4178, pp. 176 – 185, International Society for Optics and Photonics, SPIE, 2000.

[56] G. Amor, E. Roth, D. Sharon, N. Gorelik, S. Kinstlich, and S. Nagola, "Multiple MEMS mirrors synchronization techniques, modeling, and applications," in *MOEMS and Miniaturized Systems XX* (H. Zappe, W. Piyawattanametha, and Y.-H. Park, eds.), vol. 11697, pp. 76 – 88, International Society for Optics and Photonics, SPIE, 2021.

[57] C. McQueen, "Tello ros urdf," May 2019.

[58] Mirrorcle, "Mirrorcle mems mirrors - technical overview," 2009.

[59] S. Arnon, "Effects of atmospheric turbulence and building sway on optical wireless-communication systems," *Opt. Lett.*, vol. 28, pp. 129–131, Jan 2003.

[60] S. Arnon, "Optimization of urban optical wireless communication systems," *IEEE Transactions on Wireless Communications*, vol. 2, no. 4, pp. 626–629, 2003.

[61] L. C. Andrews and R. L. Phillips, "Laser beam propagation through random media, second edition," Sep 2005.

VITA

Anılcan Tosun received his B.Sc. degree from Gaziantep University, Gaziantep, Turkey in 2018. He is currently working toward the M.Sc. degree in Electrical & Electronics Engineering department, under the supervision of Prof. Murat Uysal at Ozyegin University, Istanbul, Turkey. During his graduate studies, he worked at OKATEM laboratory, Ozyegin University. His current research interests include optical wireless communication, drone-based free-space optical wireless communication.